

Advances in the Ocean Color Component of the Aerosol Robotic Network (AERONET-OC)

GIUSEPPE ZIBORDI,^a BRENT N. HOLBEN,^b MARCO TALONE,^c DAVIDE D'ALIMONTE,^d ILYA SLUTSKER,^{b,e}
DAVID M. GILES,^{b,e} AND MIKHAIL G. SOROKIN^{b,e}

^a Joint Research Centre of the European Commission, Ispra, Italy

^b National Aeronautics and Space Administration Goddard Space Flight Center, Greenbelt, Maryland

^c Barcelona Expert Centre, Institute of Marine Sciences (ICM-CSIC), Barcelona, Spain

^d AEQUORA, Lisbon, Portugal

^e Science Systems and Applications Inc., Lanham, Maryland

(Manuscript received 10 June 2020, in final form 2 November 2020)

ABSTRACT: The Ocean Color Component of the Aerosol Robotic Network (AERONET-OC) supports activities related to ocean color such as validation of satellite data products, assessment of atmospheric correction schemes, and evaluation of bio-optical models through globally distributed standardized measurements of water-leaving radiance and aerosol optical depth. In view of duly assisting the AERONET-OC data user community, this work (i) summarizes the latest investigations on a number of scientific issues related to above-water radiometry, (ii) emphasizes the network expansion that from 2002 until the end of 2020 integrated 31 effective measurement sites, (iii) shows the equivalence of data product accuracy across sites and time for measurements performed with different instrument series, (iv) illustrates the variety of water types represented by the network sites ensuring validation activities across a diversity of observation conditions, and (v) documents the availability of water-leaving radiance data corrected for bidirectional effects by applying a method specifically developed for chlorophyll-*a*-dominated waters and an alternative one that is likely suitable for any water type.

KEYWORDS: In situ oceanic observations; Instrumentation/sensors; Quality assurance/control; Remote sensing


1. Introduction

The Ocean Color Component of the Aerosol Robotic Network (AERONET-OC; appendix A provides the definitions of all acronyms used in this paper) was conceived to support ocean color activities with spectral normalized water-leaving radiance L_{WN} and aerosol optical depth τ_a data (appendix B provides a list of the definitions of all variables and symbols used in this paper) retrieved from radiometers deployed on offshore fixed structures (Zibordi et al. 2006). Following the initial field-testing of instruments and measurement protocols (Zibordi et al. 2002) and by fully relying on the AERONET infrastructure (Holben et al. 1998; Holben et al. 2001), the first AERONET-OC site was established during early 2002 at the Acqua Alta Oceanographic Tower (AAOT) in the Adriatic Sea. This deployment, concurrent with the launch of the Medium Resolution Imaging Spectrometer (MERIS) on board the *Envisat* platform, was then followed by others in different regions of the globe using constructions such as lighthouses, service structures, oil rigs (e.g., Zibordi et al. 2006). Over time, AERONET-OC has become a major source of reference measurements for the assessment of satellite ocean color data (Zibordi et al. 2009a; Moore et al. 2015; Pahlevan et al. 2017; Valente et al. 2019), atmospheric correction processes (Jamet et al. 2011; Fan et al. 2017), bio-optical models (Tan et al. 2019), data merging schemes (Mélín and Zibordi 2007) and vicarious calibration methods (Mélín and Zibordi 2010;

Hlaing et al. 2014). AERONET-OC measurement protocol, instruments calibration, data handling, processing, quality assurance, and accessibility, were amply detailed in Zibordi et al. (2009b). During the last decade, however, AERONET-OC marked incremental expansion and profited technological and application-oriented developments leading to further consolidation of the network. This work documents these latest developments and their impact on AERONET-OC data products.

2. Background

AERONET gathers field measurements from CE-318 and CE-318T radiometer systems through a variety of solutions (i.e., satellite, mobile, and Internet connections) and allows for their near-real-time data processing, archival at different quality levels (i.e., level 1.0, level 1.5, and level 2.0) and access through a web interface (see Fig. 1). Since early 2000s this central infrastructure sustained the development, expansion and consolidation of AERONET-OC whose details, spanning from measurement protocol to data access, were provided in Zibordi et al. (2009b). A number of successive focused investigations allowed for a further assessment of AERONET-OC methods and data products. A few studies of explicit relevance addressed the uncertainties of data products (Gergely and Zibordi 2014), the consistency of basic assumptions supporting the determination of L_w (Zibordi 2016), the application of

 Denotes content that is immediately available upon publication as open access.

Corresponding author: G. Zibordi, giuseppe.zibordi@ec.europa.eu

DOI: 10.1175/JTECH-D-20-0085.1



This article is licensed under a Creative Commons Attribution 4.0 license (<http://creativecommons.org/licenses/by/4.0/>).

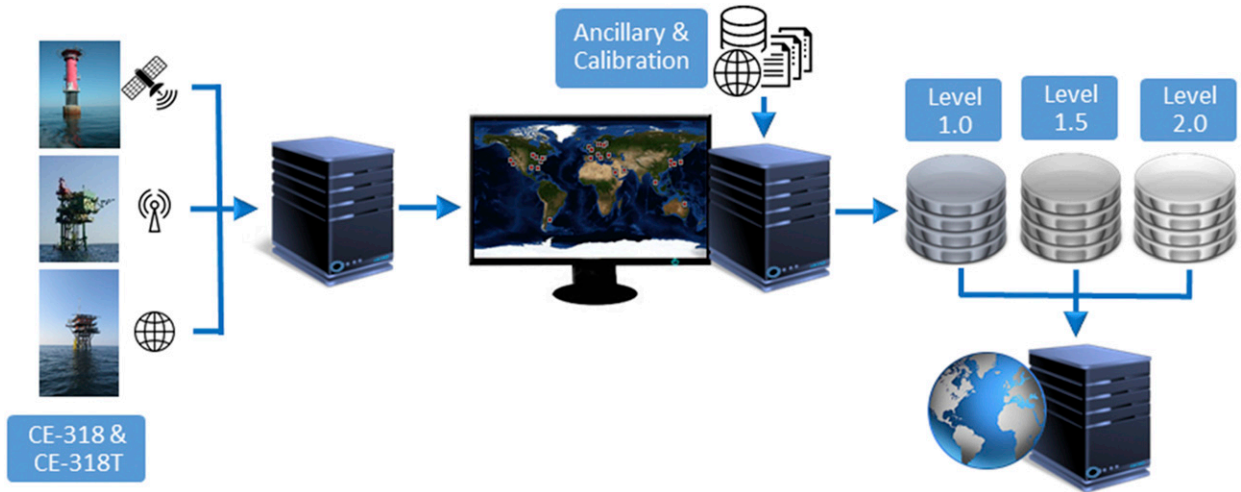


FIG. 1. Schematic of the AERONET data infrastructure. Measurements from CE-318 or CE-318T radiometer systems are ingested through satellite, mobile, or Internet connections. Near-real-time processing, supported by ancillary and calibration data, leads to the generation of data products at incremental quality levels (i.e., from level 1.0 to level 2.0), all accessible on a website.

alternative approaches for the minimization of bidirectional effects (Talone et al. 2018), the impact of spectral perturbations by deployment structures (Talone and Zibordi 2019), adjacency effects in satellite data as a function of the land/atmosphere optical properties and the distance from the coast (Bulgarelli and Zibordi 2018a). With the objective to introduce those elements supporting recent network developments, a brief summary of AERONET-OC basics is provided in the following sections together with an overview of relevant findings from latest investigations.

a. Measurement and data reduction methods

AERONET-OC quantifies the water-leaving radiance $L_w(\theta, \varphi, \lambda)$ —that is, the radiance emerging from below the water surface—from measurements of the total radiance from the sea $L_T(\theta, \varphi, \lambda)$ and of the sky radiance $L_i(\theta', \varphi, \lambda)$, according to

$$L_w(\theta, \varphi, \lambda) = L_T(\theta, \varphi, \lambda) - \rho(\theta, \varphi, \theta_0, W)L_i(\theta', \varphi, \lambda), \quad (1)$$

where θ and θ' are the viewing angles for sea and sky measurements with $\theta' = 180^\circ - \theta$, φ is the relative azimuth between solar and sensor planes, θ_0 is the solar zenith angle, λ is the center wavelength of the specific spectral band, and W is the wind speed. Note that the dependence on θ_0 is not explicitly indicated for the radiance terms. The term $\rho(\theta, \varphi, \theta_0, W)$ is the water surface reflectance factor, a function of the measurement and illumination geometries, and of the sea state expressed through W . In agreement with consolidated measurement schemes [International Ocean Colour Coordinating Group (IOCCG); IOCCG 2019], $L_T(\theta, \varphi, \lambda)$ and $L_i(\theta', \varphi, \lambda)$ values are determined at $\theta = 40^\circ$ and $\varphi = 90^\circ$. Larger values of φ (e.g., $\varphi = 135^\circ$), which may further minimize glint perturbations with respect to $\varphi = 90^\circ$ (Mobley 1999), can lead to larger superstructure perturbations with increasing θ_0 .

The values of $\rho(\theta, \varphi, \theta_0, W)$ applied in AERONET-OC data processing are those determined by Mobley (1999) at $\lambda = 550$ nm through HydroLight simulations (Mobley 1994; Mobley and

Sundman 2000) using the Cox and Munk (1954) slope distribution of surface waves. It is recalled that the theoretical sky radiance distribution, neglecting polarization effects but accounting for multiple scattering and aerosol contributions, was constructed benefitting of an irradiance model (Gregg and Carder 1990) and experimental sky radiance patterns (Harrison and Coombes 1988).

The normalized water-leaving radiance $L_{wN}(\lambda)$, the radiance that would occur with nadir view, no atmosphere, the sun at the zenith and at the mean sun–Earth distance, is computed as

$$L_{wN}(\lambda) = L_w(\theta, \varphi, \lambda)C_{ir}(\theta, \varphi, \theta_0, \lambda, \tau_a, IOP, W)[D^2t_d(\lambda)\cos\theta_0]^{-1}, \quad (2)$$

where $D^2t_d(\lambda)\cos\theta_0$ is an estimate of the irradiance ratio of downward $E_d(\lambda)$ to mean extra-atmospheric $E_0(\lambda)$ (Zibordi et al. 2004), with D accounting for the sun–Earth distance as a function of the day of the year and $t_d(\lambda)$ being the atmospheric diffuse transmittance (Deschamps et al. 1983). The correction factor $C_{ir}(\theta, \varphi, \theta_0, \lambda, \tau_a, IOP, W)$ minimizes the impact of bidirectional effects that are due to the nonnadir view of the field radiometer and of the illumination geometry, with τ_a and IOP indicating the aerosol optical depth and the inherent optical properties of water, respectively (see details in section 3).

AERONET-OC, in agreement with AERONET requirements, relies on CE-318 and the more recent CE-318T radiometers conceived to perform multispectral measurements in the ultraviolet, visible and near-infrared spectral regions with a full-angle field of view of 1.2° . Specifically, CE-318 and CE-318T radiometer systems configured for ocean color applications and called the Sea-Viewing Wide Field-of-View Sensor (SeaWiFS) Photometer Revision for Incident Surface Measurements (SeaPRISM), autonomously acquire on a channel-by-channel basis (i.e., spectrally asynchronously) the following:

- (i) the direct solar irradiance $E(\theta_0, \varphi_0, \lambda)$ as a function of θ_0 , solar azimuth angle φ_0 , and λ to determine the aerosol spectral optical depth $\tau_a(\lambda)$ required to compute $t_d(\lambda)$;

- (ii) N_T sea-radiance measurements for determining $L_T(\theta, \varphi, \lambda)$;
- (iii) N_i sky-radiance measurements for determining $L_i(\theta', \varphi, \lambda)$.

The sky and sea measurements for determining $L_i(\theta', \varphi, \lambda)$ and $L_T(\theta, \varphi, \lambda)$ are performed with $N_i = 3$ and $N_T = 11$, respectively. The larger number of N_T measurements with respect to N_i , is suggested by the need to statistically address the impact of wave perturbations. Measurements are not performed in the presence of clouds affecting $E(\theta_0, \varphi_0, \lambda)$.

For each measurement sequence, $L_i(\theta', \varphi, \lambda)$ is determined by simply averaging the N_i sky-radiance data. Conversely, $L_T(\theta, \varphi, \lambda)$ is determined from the average of a fixed percent of the N_T sea-radiance measurements exhibiting the lowest radiance levels (i.e., 2 out of 11). This approach has been suggested by studies (Zibordi et al. 2002; Hooker et al. 2002) highlighting the need for aggressive filtering of above-water measurements to minimize the effects of wave perturbations in $L_T(\theta, \varphi, \lambda)$.

Equivalent to AERONET atmospheric data products (Holben et al. 2001), ocean color data are also archived at three incremental quality levels. Level 1.0 only includes $L_{\text{WN}}(\lambda)$ data for which (i) $L_i(\theta', \varphi, \lambda)$ and $L_T(\theta, \varphi, \lambda)$ are determined from measurement sequences not exhibiting missing data; (ii) the dark values are below a given threshold; (iii) the value of φ_0 is within site-dependent limits to minimize superstructure perturbations in $L_T(\theta, \varphi, \lambda)$; (iv) $\tau_a(\lambda)$ has been determined; and (v) W is below the maximum threshold of 15 m s^{-1} .

Level 1.5 includes $L_{\text{WN}}(\lambda)$ derived from level 1.0 data for which (i) cloud screened AERONET $\tau_a(\lambda)$ exist at level 1.5 in the AERONET database (Smirnov et al. 2000; Giles et al. 2019); (ii) a series of empirical thresholds are satisfied (e.g., $L_{\text{WN}}(\lambda) > -0.01 \text{ mW cm}^{-2} \mu\text{m}^{-1} \text{ sr}^{-1}$ indicating absence of exceedingly negative values at any λ); $L_{\text{WN}}(412) < L_{\text{WN}}(443)$ for coastal sites; $L_{\text{WN}}(1020) < 0.1 \text{ mW cm}^{-2} \mu\text{m}^{-1} \text{ sr}^{-1}$, except for sites exhibiting very turbid waters, to exclude measurements appreciably affected by the presence of obstacles in the sight of the sea-viewing sensor; and (iii) the N_T sea-radiance measurements and N_i sky-radiance measurements exhibit low variance indicating low wave perturbations and negligible cloud contamination, respectively. Specifically, the test on the variance of the N_T sea-radiance data removes measurement sequences affected by random high radiance values due to glint or foam reflectance. The test on the variance of the N_i sky-radiance data, in combination with the AERONET cloud screening for $\tau_a(\lambda)$, aims at removing those measurement sequences likely perturbed by clouds that may hinder the determination of $L_i(\theta', \varphi, \lambda)$ and consequently decrease the accuracy of $L_{\text{WN}}(\lambda)$. Still, additional perturbations weakening the assumption of clear sky, may result from sparse clouds not affecting the sun disk and the portion of sky in the direction (θ', φ) . Nevertheless, it is expected that uncertainties resulting from those unfavorable measurement conditions are (at least partially) accounted for by the uncertainties assigned to $t_d(\lambda)$ and to environmental perturbations (see Zibordi et al. 2009b).

Level 2.0 data include $L_{\text{WN}}(\lambda)$ determined from level 1.5 products for which (i) the level 2.0 AERONET $\tau_a(\lambda)$ exist; (ii)

the N_T sea-radiance measurements and N_i sky-radiance measurements satisfy lower variance thresholds with respect to those applied for level 1.5 (details on these thresholds are provided in section 3); (iii) the differences between pre- and postdeployment calibration coefficients for the AERONET-OC radiometer exhibit values smaller than 5% (it is mentioned that generally these differences do not exceed 1% per year); and (iv) $L_{\text{WN}}(\lambda)$ do not show questionable values during the final spectrum-by-spectrum assessment performed by a practiced analyst. This final step has been often supported by an automatic process (D'Alimonte and Zibordi 2006) aiming at rejecting $L_{\text{WN}}(\lambda)$ spectra exhibiting (i) low statistical representativeness within the dataset itself (*self-consistency* test) and (ii) anomalous features with respect to a reference set of quality-checked data (*relative-consistency* test). The automatic procedure has been effectively applied to data from a variety of sites (see Zibordi et al. 2009b). However, the analysis of results has shown limits in addressing unique measurement conditions not represented in both the reference dataset or the AERONET-OC data going to be screened. Because of this, the supervised spectrum-by-spectrum quality check is still the fundamental step toward level 2.0 data quality.

Statistically, approximately 44% of the level 1.0 $L_{\text{WN}}(\lambda)$ are raised to level 1.5 and only 28% of the level 1.0 $L_{\text{WN}}(\lambda)$ are qualified for level 2.0, as determined with data from 2002 until mid-2019 for which $L_{\text{WN}}(\lambda)$ values have been available at all quality levels for the major sites.

b. Calibration

Calibrations of each AERONET-OC radiometer system comprise independent actions performed at the Goddard Space Flight Center of the National Aeronautics Space Administration (NASA GSFC) for direct solar irradiance and radiance measurements.

Pre- and postdeployment calibrations for direct solar irradiance are obtained indirectly by relying on a reference instrument in turn calibrated through the Langley method (Holben et al. 1998). Pre- and postdeployment calibrations for radiance measurements, which are relevant to above-water radiometry, are performed using an integrating sphere (IOCCG 2019). These derived pre- and postdeployment calibration coefficients are interpolated over time to account for any sensitivity change of the radiometers during field operation. All calibration measurements and retrieved coefficients are permanently stored in the AERONET database.

Fully independent radiance calibrations performed at the Joint Research Centre (JRC) on a number of AERONET-OC radiometers (tentatively $1/3$ of those annually deployed), add a further check to the overall quality process. These independent radiance calibrations rely on the use of National Metrology Institutes (NMI) traceable 1000 W FEL lamps and reference 99% reflectance plaques (IOCCG 2019).

Verification of the accuracy of both NASA GSFC and JRC absolute radiance calibrations were performed by the National Institute of Standards and Technology (NIST) using a CE-318 radiometer. Results indicate uncertainties

within approximately 1% in the visible spectral region of major interest for ocean color applications (Johnson et al. 2021).

Also, since 2010 the temperature sensitivity was characterized for each instrument at all spectral bands (Giles et al. 2019). This process has mostly led to an increase of the accuracy for τ_a determined from the near-infrared spectral bands (i.e., 870 and 1020 nm). Still, it does not have an appreciable impact on the determination of τ_a and L_{WN} in the visible spectral region.

c. Uncertainties

Uncertainties are a fundamental aspect of any measurement and are essential for a confident application of data products. In the case of AERONET-OC, a quantification of $L_{\text{WN}}(\lambda)$ uncertainties was proposed in Zibordi et al. (2009b). These uncertainties were provided in relative terms (i.e., in percent) making explicit reference to the AAOT site representative of a variety of measurement conditions. The analysis embraced uncertainty contributions from absolute radiance calibrations, sensitivity decay during deployments, corrections for bidirectional effects, water surface reflectance, atmospheric diffuse transmittance, environmental perturbations (sky radiance variability and wave effects). Assuming each uncertainty independent from the others, their combined spectral values resulting from the quadrature sum of the various contributions, lead to values approaching 5% in the blue–green spectral regions and 8% in the red.

The former results provide a term of reference for typical relative uncertainties affecting $L_{\text{WN}}(\lambda)$ AERONET-OC data. Still, these uncertainty values may not equally apply to measurements performed with observation conditions significantly different from those characterizing the AAOT site. The issue has been addressed following the Guide to the Expression of Uncertainty in Measurement (GUM) by quantifying uncertainties affecting data products from a number of AERONET-OC sites. Results from Gergely and Zibordi (2014) indicate the following:

- (i) The relative uncertainties determined for AAOT $L_{\text{WN}}(\lambda)$ through the application of GUM accounting for correlations among the various uncertainty contributions, confirm within 0.5% the values earlier provided in Zibordi et al. (2009b). The study also shows a reduction of uncertainties when excluding the highest values of solar zenith angle and of aerosol optical depth.
- (ii) The relative uncertainties may amply vary from site to site as a function of the water type, which implies different spectral shapes and ranges of $L_{\text{WN}}(\lambda)$. These relative uncertainties may largely exceed the 5% threshold

commonly considered for validation activities (Zibordi and Voss 2014).

- (iii) The absolute uncertainties affecting $L_{\text{WN}}(\lambda)$ also appreciably vary from site to site, but they do not necessarily mirror the values of relative uncertainties. In particular, sites exhibiting relative uncertainties well above those determined for the AAOT site, may exhibit much lower absolute uncertainties.

The above findings are summarized in Table 1 for two AERONET-OC sites: the AAOT characterized by moderately sediment-dominated waters and the Helsinki Lighthouse (HLT) characterized by waters dominated by high concentrations of colored dissolved organic matter (CDOM). Remarkable are the differences between relative and absolute uncertainties, more pronounced in the blue and green spectral bands. Just considering the 412 nm center wavelength, the relative uncertainties for AAOT and HLT determined with GUM exhibit values of 5.1% and 27.4%, respectively (i.e., much lower for the AAOT site). On the contrary, the absolute uncertainties show values of 0.038 and 0.016 $\text{mW cm}^{-2} \mu\text{m}^{-1} \text{sr}^{-1}$ at 412 nm for AAOT and HLT, respectively (i.e., much lower for the HLT site). Definitively, the median of the $L_{\text{WN}}(\lambda)$ spectral values contributing to the analysis provided in Table 1, well explains the differences: the $L_{\text{WN}}(\lambda)$ median at 412 nm is one order of magnitude higher for the AAOT than for HLT data.

Aside from suggesting the need to compute uncertainties for each specific AERONET-OC site, the above results confirm the importance of determining both relative and absolute uncertainties, whose values are expected to be representative for the range of considered radiances.

d. Products assessment

AERONET-OC $L_{\text{WN}}(\lambda)$ rely on the basic measurement equation defined by Eq. (1) and a relatively small number of data collected with a narrow field of view (i.e., 1.2° full angle). The major drawback, however, arises from the spectrally asynchronous measurement capability of CE-318 and CE-318T radiometers: measurements are performed at different time for each spectral band. While this technical aspect is not relevant for sky or sun measurements benefitting of sources (i.e., sun and sky) relatively stable over a short time during clear sky conditions, it definitively affects sea measurements as a result of wave perturbations implicitly leading to differences in surface perturbations across the various bands.

The measurement capabilities offered by CE-318 and CE-318T systems are thus far away from being ideal for ocean color field applications (IOCCG 2019). Still, strict quality assurance of the

TABLE 1. Relative (u_r ; %) and absolute (u_a ; $\text{mW cm}^{-2} \mu\text{m}^{-1} \text{sr}^{-1}$) uncertainties determined for $L_{\text{WN}}(\lambda)$ from the AAOT and HLT sites at nominal center wavelengths from 412 to 667 nm [after Gergely and Zibordi (2014)]. The symbol m indicates the median of the $L_{\text{WN}}(\lambda)$ spectra ($\text{mW cm}^{-2} \mu\text{m}^{-1} \text{sr}^{-1}$) included in the uncertainty analysis.

	412			443			488			551			667		
	u_r	u_a	m	u_r	u_a	m	u_r	u_a	m	u_r	u_a	m	u_r	u_a	m
AAOT	5.3	0.038	0.71	4.8	0.043	0.87	4.6	0.056	1.20	4.9	0.049	1.00	7.3	0.010	0.13
HLT	27.4	0.016	0.06	13.7	0.014	0.10	7.8	0.017	0.22	6.7	0.026	0.39	6.9	0.008	0.12

measurement sequences can lead to data products meeting requirements for validation activities. As stated in section 1, an early step of the quality assurance process, which includes a number of quality control checks, is the removal of any measurement sequence exhibiting variance above given thresholds in the total radiance from the sea in at least one spectral band (Zibordi et al. 2009b). This means that quality assured measurement sequences raised to level 1.5 and level 2.0 are not affected by large surface perturbations. As a result of the filtering applied, AERONET-OC $L_{\text{WN}}(\lambda)$ are only determined for low-to-mild sea state conditions bound by wind speeds typically not exceeding 5 m s^{-1} . Direct benefit of such quality assurance process is thus the low variability of the water surface reflectance factor ρ as a function of wind speed across a wide range of solar zenith angles (Zibordi 2016).

The measurement sequences passing the former quality assurance step might still be affected by excessive glint resulting from the reflection of sky radiance from brighter portions of the sky. Because of this, as already anticipated, $L_T(\theta, \varphi, \lambda)$ is determined from each quality assured measurement sequence by averaging a percent of the N_T data exhibiting the lowest radiance values in each band. The use of the average of the lowest radiance values instead of the mean of all values, still supported by experimental evidence (Zibordi 2012, 2016; Pitarch et al. 2020), might be responsible for an underestimate of $L_{\text{WN}}(\lambda)$ more pronounced at low solar zenith angles θ_0 (i.e., below 20°) and increasing with the wind speed. Table 2 summarizes comparison results between $L_{\text{WN}}(\lambda)$ from AERONET-OC and in-water measurements. These results show an excellent agreement between the independent determinations of $L_{\text{WN}}(\lambda)$, nevertheless limited to cases with $\theta_0 > 20^\circ$ and benefitting of glint filtering (i.e., not including measurement sequences heavily affected by surface perturbations and consequently mostly restricted to relatively low wind speeds). Still, recognizing the lack of a fundamental element justifying the use of the mean of relative minima alternative to the mean of all values, the agreement of the data shown in Table 2 is largely explained by the combined uncertainties of the compared measurements and corroborate the applied AERONET-OC processing scheme.

e. Polarization effects

A number of recent studies highlighted the dependence of above-water radiometry on polarization effects (Harmel et al. 2012; Mobley 2015; Hieronymi 2016; D'Alimonte and Kajiyama 2016; Foster and Gilerson 2016; Zhang et al. 2017; Gilerson et al. 2018). Recognizing that an operational network such as AERONET-OC can only rely on consolidated findings, an effort was made to evaluate the impact of polarization through tabulated values of ρ determined accounting (Mobley 2015) and not accounting (Mobley 1999) for polarization effects. The analysis was performed by comparing AERONET-OC $L_W(\lambda)$ data determined using the different ρ values with $L_W(\lambda)$ from independent in-water measurements (Zibordi 2016). Results, restricted to the measurement conditions for which AERONET-OC data can be produced (i.e., wind speeds generally lower than 5 m s^{-1}) indicated a slightly better performance of $L_W(\lambda)$ determined without accounting for polarization effects and justifies the

TABLE 2. Comparison results between $L_{\text{WN}}(\lambda)$ from AERONET-OC and independent in-water measurements accounting for 185 matchups at various center wavelengths in the 412–667-nm spectral interval [after Zibordi (2016)]. The symbol ψ indicates the mean of signed percent differences (i.e., an index for the bias affecting the compared data) of AERONET-OC-derived $L_{\text{WN}}(\lambda)$ with respect to in-water data products. The symbol $|\psi|$ indicates the mean of absolute percent differences (i.e., an index for the dispersion of data).

	412	443	488	547	667
ψ	0	+1	+1	+3	+3
$ \psi $	7	6	6	5	18

current application of the ρ values from Mobley (1999). Still, alternative ρ values, hopefully accounting for their spectral dependence, can be applied as soon as available and supported by community consensus.

f. Bidirectional effects

The nonisotropy of the in-water light field implies the correction of $L_W(\theta, \varphi, \lambda)$ data for bidirectional effects due to the solar zenith angle and the nonnadir view of the sensor. The correction approach commonly applied for bidirectional effects is that proposed for Case-1 (i.e., chlorophyll-*a* dominated) waters by Morel et al. (2002) hereinafter called Chla based. Considering that most of the AERONET-OC sites are located in optically complex coastal waters, the corrections relying on the Chla-based approach are likely affected by large uncertainties. Because of this, alternative corrections applicable to both Case-1 and optically complex waters have been evaluated with a view to their applicability to AERONET-OC data.

Among the various approaches proposed in literature (e.g., Park and Ruddick 2005), the one considered for dedicated investigations was that by Lee et al. (2011). This correction, hereinafter called IOP-based, provides the major advantage of relying on the retrieval of water IOPs from $L_W(\theta, \varphi, \lambda)$ itself. An experimental study focused on the comparison of Chla- and IOP-based approaches, still restricted to the bidirectional effects due to nonnadir view, shows average relative differences of corrections varying between 10% and 40% in the blue and green spectral regions with standard deviation of 10%–25% (Talone et al. 2018). By using in situ reference data to quantify the uncertainties affecting the correction factors from the two approaches, the study indicates relative spectrally and water dependent uncertainties varying between 20% and 60% for the Chla-based approach, with the highest values affecting the blue and red regions. Conversely, the IOP-based approach shows relative uncertainties within 20%–35% and lower dependence on wavelength and water type. These results have motivated the implementation of the IOP-based correction approach in the AERONET-OC processing in addition to the Chla-based one.

g. Perturbations by deployment structures

AERONET-OC radiometers are deployed on fixed platforms. The location of the instrument on each platform needs to ensure the minimization of structure perturbations. This implies identifying locations ideally free from obstacles above

the radiometer, and allowing the sight of view of the sensor to point at the water surface well away from the main structure during the central hours of the day when satellite overpasses occur (at least for deployments underpinning ocean color validation activities). The former requirement may face challenges due to the size and shape of structures, deployment restrictions due to the presence of obstacles or of highly reflective objects. An early investigation carried out at the AAOT (Hooker and Zibordi 2005) indicated that observations performed pointing at the water surface at a distance at least as large as the height of the deployment structure would minimize perturbations due to the structure itself. This finding, also supported by field measurements performed on a research vessel (Hooker and Morel 2003), was proposed as a practical rule. However, its widespread applicability has not been demonstrated. In particular, the spectral impact of superstructures in $L_{WN}(\lambda)$ remained an open issue. This latter point has been tackled in a recent investigation performed at the AAOT by collecting above-water radiometry data at various distances from the structure adopting the AERONET-OC viewing geometry (i.e., $\theta = 40^\circ$ and $\varphi = 90^\circ$) with the deployment platform exhibiting its regular appearance, or alternatively covered by white sheets (Talone and Zibordi 2019).

Results from this investigation indicate that for the low reflectance case (i.e., the AAOT without white cover), the structure perturbations affect $L_{WN}(\lambda)$ by less than 1% in the visible spectral region when the sea-radiance measurements are performed at distances from the structure larger than the height of the structure itself. However, they may exceed 2% beyond 800 nm. For identical measurement geometries, but for the high reflectance case (i.e., the AAOT with white cover), results show that the impact of the superstructure approaches 1% in the blue-green and may exceed 2% beyond approximately 600 nm. Recognizing that the strict applicability of these results is confined to a specific deployment platform, still, these findings confirm previous deployment recommendations and additionally provide new elements for the quantification of spectral uncertainties affecting data products.

h. Adjacency effects

AERONET-OC sites are almost totally located in coastal regions. This particular condition, generally depending on the larger availability of fixed structures in coastal rather than open sea, may impact the exploitation of data products in validation processes. In fact, close regions exhibiting different surface reflectance such as sea and land, naturally lead to adjacency effects in top-of-the-atmosphere data (Bulgarelli and Zibordi 2018a). A number of targeted studies (e.g., Bulgarelli and Zibordi 2018b) showed that adjacency effects may lead to unwanted perturbations in satellite data products up to more than 10 n mi (1 n mi = 1.852 km) away from the coast. These perturbations, which spectrally vary with the reflectance of land surfaces, water type, illumination and viewing geometries, coastline and the specific atmospheric correction method applied, may become responsible for seasonal trends in satellite data (Bulgarelli et al. 2018). Recognizing that adjacency effects only concern satellite data products, still, the application of AERONET-OC data from sites located within a very few

nautical miles from the coast may be challenged in validation activities not supported by schemes allowing to remove adjacency perturbations in remote sensing data. This stresses the need to establish AERONET-OC sites at locations well away from the coast when prioritizing support to ocean color validation activities. Nevertheless, time series of AERONET-OC data from regions located within a few nautical miles from the coast are expected to gather increased value when operational atmospheric correction codes will include schemes for the minimization of adjacency effects.

3. An overview on network advances

Aside from a constant increase of the measurement sites across a variety of water types all over the globe, AERONET-OC has incrementally benefitted of investigations such as those on the minimization of bidirectional effects and on technological progresses allowing to expand the number of spectral bands from 9 to 12. Following the release of the version-3 AERONET database (Giles et al. 2019; https://aeronet.gsfc.nasa.gov/new_web/ao_t_levels_versions.html), the parallel AERONET-OC processing for the version-3 database has incorporated those advances and in the future is expected to also integrate progresses on calibration, data reduction and quality assurance/control. The recent main network advances are detailed in the following subsections.

a. Instrument and band setting

Excluding some early CE-318 analog radiometer systems, most AERONET-OC deployments rely on CE-318 9-channel digital systems and on the recent CE-318T 12-channel ones.

Table 3 shows the reference center wavelengths for the 9-channel and 12-channel systems. The CE-318 9-channel radiometer system largely exhibits spectral bands corresponding to those of the Moderate Resolution Imaging Spectroradiometer (MODIS) and the Visible Infrared Imaging Radiometer Suite (VIIRS) satellite sensor. Conversely, the CE-318T 12-channel system exhibits bands matching most of the Ocean Land Color Instrument (OLCI) and it is definitively expected to overlap the major ocean color ones of the forthcoming Plankton, Aerosol, Cloud, and Ocean Ecosystem (PACE) mission.

Also relevant, considering the growing interest in remote sensing applications focusing on lake waters (e.g., Moore et al. 2019), is that the 12-channel standard system has been conceived with two different spectral band settings: one for marine applications and the other more suitable for inland waters.

Briefly, the CE-318T radiometer system for marine applications, when compared with the CE-318 version, features additional spectral bands centered at 400, 510, 620, and 779 nm. While the supplemental bands in the visible allow for a more comprehensive spectral determination of $L_{WN}(\lambda)$, the band centered at 779 nm combined with that at 865 nm allow for investigating $\tau_a(\lambda)$ at center wavelengths equivalent to those commonly supporting the atmospheric correction of satellite ocean color data.

The CE-318T radiometer system for inland water applications, when compared to the marine one, has spectral bands centered at 681 and 709 nm replacing those at 400 and 779 nm. The spectral setting comprising the 667, 681 and 709 nm center

TABLE 3. Corresponding nominal center wavelengths λ (nm) of CE-318 9-channel and CE-318T 12-channel radiometer systems (all having 10-nm bandwidth), in comparison with those of recent satellite ocean color sensors (OLCI, VIIRS, and MODIS). The symbols s and i indicate the marine and inland water spectral band configurations, respectively.

	λ													
CE-318T (s)	400	412.5	442.5	490	510	560	620	667			779	865	940	1020
CE-318T (i)		412.5	442.5	490	510	560	620	667	681	709		865	940	1020
CE-318		412	443	488	531	551		667				870	940	1020
OLCI	400	412.5	442.5	490	510	560	620	667	681	709	779	865	940	1020
VIIRS		412	445	488		555		672				865		
MODIS		412.5	443	488	531	551		667	678			870	940	

wavelengths aims at supporting the detection and quantification of phytoplankton blooms in the near-surface water layer.

While the foreoptics, optics and detector components of CE-318 and CE-318T radiometers are substantially the same for the relevant visible and near-infrared spectral bands, the CE-318T units exhibit an improved analog-to-digital resolution (21 versus 16 effective bits of the CE-318 units). Additionally, CE-318T systems can transmit relatively large volumes of data through General Packet Radio Service (GPRS) [opposite to the limited capability of satellite data collection platforms (DCP)]. Further relevant feature of the new CE-318T systems is the possibility to store large volumes of data (up to 32 gigabytes) on Secure Digital (SD) cards, definitely relevant for remote sites not always within GPRS coverage and constrained by the low transmission rate of DCP (Zibordi et al. 2009b).

CE-318T systems also exhibit some measurement protocol improvement with respect to the former CE-318 version. First, the sign of the relative azimuth φ can be varied during the day or across the year (e.g., from -90° to $+90^\circ$). This feature is relevant for structures with deployment locations that may not allow respecting the basic geometric requirements during the full day or during part of the year. It is mentioned that the parameters determining the measurement geometry (i.e., θ and φ , in addition to the exact center wavelengths of the instrument) are accessible in each data record at any quality level.

An additional major feature of the CE-318T systems is the capability of performing an increased number of above-water marine or lake measurement sequences. By recalling that for CE-318 systems the number of above-water measurements is limited to a single sequence every 30 min, the marine or lake sequences of relevant measurements performed with CE-318T systems can now be increased by up to a factor of 3, with each sequence completed in 5 min. This may allow producing measurement replicates at a finer temporal scale, relevant to enhance the quality assurance of data and better quantify the environmental perturbations contributing to $L_{WN}(\lambda)$ uncertainties.

b. Sites

Figure 2 displays the location of the 31 AERONET-OC sites to date. Notable, while the Northern Hemisphere exhibits a substantial midlatitude distribution of sites across continents, the Southern Hemisphere shows a very few active ones. The marine sites represent a number of water types embracing chlorophyll- a -, sediment-, and CDOM-dominated waters. When considering the lake sites, they embrace a variety of inland

waters characterized by different seasonal conditions including the occurrence of harmful algal blooms. Finally, note the number of decommissioned marine sites. This is mostly an indication of the difficulty to maintain access to offshore locations often implying complex logistics and extraordinary safety measures governed by agreements with nonresearch bodies owning the structures.

The temporal expansion of the AERONET-OC sites is illustrated in Fig. 3 together with the satellite ocean color missions that mostly benefit from the network data. Table 4 provides the comprehensive list of AERONET-OC sites (to date) together with details on location, type of structure and responsible institution.

c. Processing

A number of changes have been implemented in the AERONET-OC processing supporting the version-3 database. A primary feature of the new processing release, when compared to the previous one supporting the version-2 database, is the capability to handle data from the CE-318T 12-channel instruments in addition to the CE-318 9-channel ones. This does not simply imply the need for handling a higher number of spectral bands, but also the necessity to address the impact of a larger number of spectral values on the quality assurance process or, to deal with an increased number of spectrally resolved parameters such as the correction factors for bidirectional effects.

The $L_{WN}(\lambda)$ data in the version-2 database relied on the application of spectral thresholds to the standard deviations of the N_T sea-radiance measurements and N_i sky-radiance measurements, identical for both level 1.5 and level 2.0. These spectral thresholds constrained in the range of $0.1\text{--}0.2\text{ mW cm}^{-2}\mu\text{m}^{-1}\text{ sr}^{-1}$ for the N_T sea-radiance measurements and in the range of $0.02\text{--}0.03\text{ mW cm}^{-2}\mu\text{m}^{-1}\text{ sr}^{-1}$ for the N_i sky-radiance measurements, were determined from the analysis of data collected at the AAOT over a variety of water types during ideal observation conditions: clear sky and low-to-mild sea state. It is mentioned that the standard deviation of CE-318 and CE-318T radiance measurements determined with a stable laboratory source is generally lower than 0.002 and $0.001\text{ mW cm}^{-2}\mu\text{m}^{-1}\text{ sr}^{-1}$, respectively, in the spectral range of interest.

As already stated, the application of thresholds to the standard deviation of successive acquisitions aims at removing any data record likely (i) affected by significant wave perturbations or foam making difficult the application of an accurate surface reflectance factor ρ for the determination of the sky glint contribution or (ii) perturbed by clouds in the direction (θ' , φ).

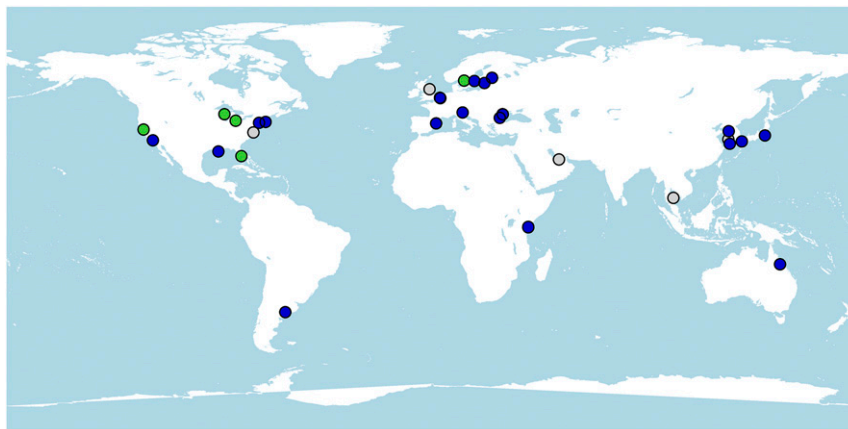


FIG. 2. Location of current AERONET-OC sites contributing to the version-3 database (https://aeronet.gsfc.nasa.gov/ocean_color.html). The blue, green, and gray filled circles indicate the active marine water, inland water, and decommissioned sites, respectively.

Obviously, an increase in the number of spectral bands naturally enhances the probability of excluding measurement sequences just because data at a single spectral band do not meet requirements. Aiming at preserving the same rigor characterizing level 2.0 $L_{WN}(\lambda)$ in the version-2 database (i.e., level 2.0 is the quality level suggested for the validation of satellite data products), level 2.0 $L_{WN}(\lambda)$ data in the version-3 database have been obtained applying the same thresholds declared above. Conversely, level 1.5 $L_{WN}(\lambda)$ data in the version-3 database have been obtained by relaxing (i.e., doubling) the thresholds. This solution provides the advantage of increasing by some percent (depending on the site) the number of $L_{WN}(\lambda)$ data at level 1.5 in the version-3 database at the expense of an

increased uncertainty due to environmental perturbations. This revision of the processing scheme is solely supported by the assumption that an increase of the number of data at level 1.5, despite a potentially lower accuracy, may provide benefit to a variety of real-time applications spanning from early assessment of satellite data products to water quality monitoring.

The AERONET-OC version-2 database relied on the Chla-based approach specifically proposed to minimize bidirectional effects in Case-1 waters (Morel et al. 2002). The related lookup tables to compute the correction factors applied to CE-318 data, however, exhibit spectral limitations. In fact the f/Q table by Morel et al. (2002) hereinafter identified as f/Q -2002, are restricted to key ocean color center wavelengths (i.e., 412, 443,

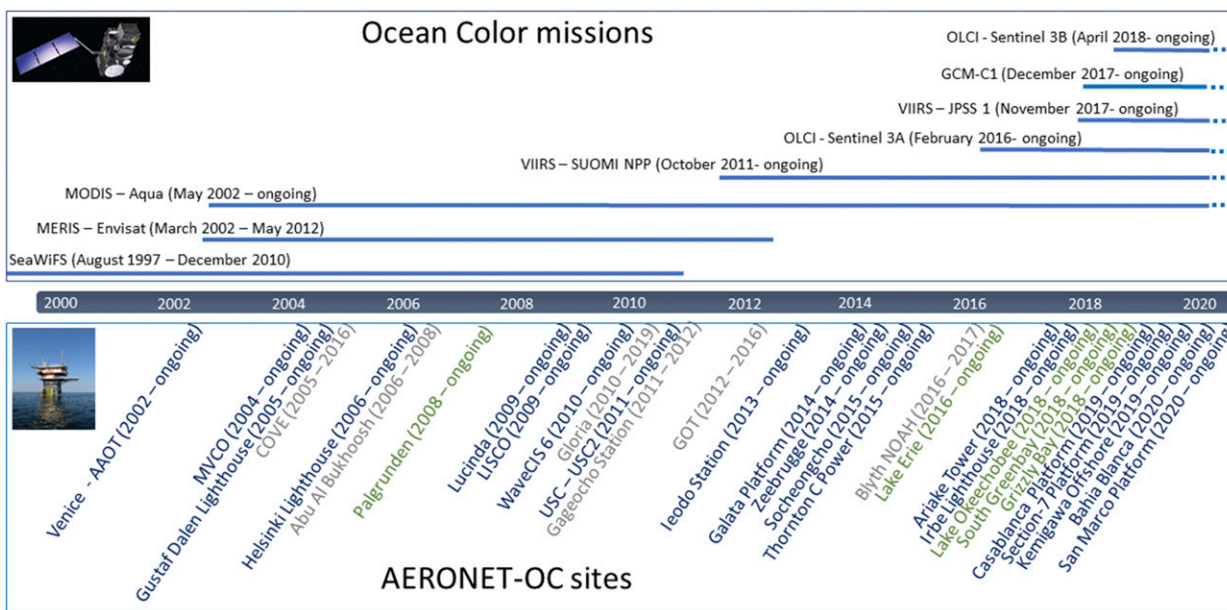


FIG. 3. (bottom) Temporal expansion of the AERONET-OC sites from 2002 until 2020 in comparison with (top) the major satellite ocean color missions supported by the network. The blue, green, and gray colors indicate the active marine water, inland water, and decommissioned AERONET-OC sites, respectively.

TABLE 4. AERONET-OC sites contributing to the version-3 database (to date). Here, EU indicates the European Union, US indicates the United States, and UK indicates the United Kingdom.

Site	Region	Lat	Lon	Structure	Responsible institutions
Venise-AAOT (2002–ongoing)	Adriatic Sea	45.314°N	12.508°E	Oceanographic tower	Joint Research Centre (EU)
MVCO (2004–ongoing)	Mid-Atlantic Bight	41.325°N	70.567°W	Oceanographic tower	University of New Hampshire (US)
Gustav Dalen Lighthouse (2005–ongoing)	Baltic proper	58.594°N	17.467°E	Lighthouse	Joint Research Centre (EU)
COVE (2005–16)	Mid-Atlantic Bight	36.900°N	75.710°W	Lighthouse	National Aeronautics and Space Administration (US)
Helsinki Lighthouse (2006–ongoing)	Gulf of Finland	59.949°N	24.926°E	Lighthouse	Joint Research Centre (EU)
Abu Al Bukhoosh (2006–08)	Persian Gulf	25.495°N	53.146°E	Oil platform	Joint Research Centre (EU)
Palgrundren (2008–ongoing)	Lake Vänern	58.753°N	13.158°E	Lighthouse	University of Stockholm (Sweden)
Lucinda (2009–ongoing)	Coral Sea	18.519°S	146.385°E	Offshore jetty	CSIRO (Australia)
LISCO (2009–ongoing)	Long Island Sound	40.955°N	73.342°W	Shore platform	City College of New York (US)
WaveCIS CSI 6 (2010–ongoing)	Gulf of Mexico	28.867°N	90.483°W	Oil platform	Louisiana State University (US)
Gloria (2011–19)	Western Black Sea	44.600°N	29.360°E	Gas platform	Joint Research Centre (EU)
USC–USC2 (2011–ongoing)	U.S. Pacific Coast	33.564°N	118.118°W	Oil platform	University of Southern California (US)
Gageocho (2011–12)	Yellow Sea	33.942°N	124.593°E	Oceanographic tower	Korea Ocean Research and Development Institute (South Korea)
GOT (2012–16)	Gulf of Thailand	09.285°N	101.407°E	Oil platform	National Aeronautics and Space Administration (US)
Ieodo Station (2013–ongoing)	Yellow Sea	32.123°N	125.182°E	Oceanographic tower	Korea Ocean Research and Development Institute (South Korea)
Galata Platform (2014–ongoing)	Western Black Sea	43.045°N	28.193°E	Gas platform	Joint Research Centre (EU)
Zeebrugge (2014–ongoing)	North Sea	51.362°N	3.120°E	Service platform	Royal Belgian Institute for Natural Sciences (Belgium)
Socheongcho (2015–ongoing)	Yellow Sea	37.423°N	124.74°E	Oceanographic tower	Korea Ocean Research and Development Institute (South Korea)
Thornton C-Power (2015–18)	North Sea	51.533°N	2.955°E	Service platform	Royal Belgian Institute for Natural Sciences (Belgium)
Blyth NOAH (2016–17)	North Sea	55.146°N	1.4209°	Lighthouse	University of Hull (UK)
Lake Erie (2016–ongoing)	Lake Erie	41.826°N	83.194°W	Lighthouse	University of New Hampshire (US)
Ariake Tower (2018–ongoing)	Ariake Sea	33.104°N	130.272°E	Service platform	Nagoya University (Japan)
Irbe Lighthouse (2018–ongoing)	Gulf of Finland	57.751°N	21.723°E	Lighthouse	Joint Research Centre (EU)
Lake Okeechobee (2018–ongoing)	Lake Okeechobee	26.902°N	80.789°W	Service platform	National Aeronautics and Space Administration (US)
South Green Bay (2018–ongoing)	Lake Michigan	44.596°N	87.951°W	Service platform	National Aeronautics and Space Administration (US)
Grizzly Bay (2019–ongoing)	Grizzly Bay	38.108°N	122.056°W	Service platform	National Aeronautics and Space Administration (US)
Casablanca Platform (2019–ongoing)	Western Mediterranean Sea	40.717°N	1.358°E	Oil platform	Joint Research Centre (EU)
Section-7 Platform (2019–ongoing)	Western Black Sea	44.546°N	29.447°E	Gas platform	Joint Research Centre (EU)
Kemigawa Offshore (2019–ongoing)	Tokyo Bay	35.611°N	140.023°E	Service platform	Yokohama National University (Japan)
Bahia Blanca (2020–ongoing)	Bahia Blanca	39.148°S	61.722°W	Service platform	Universidad Nacional del Sur (Argentina)
San Marco Platform (2020–ongoing)	Western Indian Ocean	2.942°S	40.215°E	Launching platform	Joint Research Centre (EU)

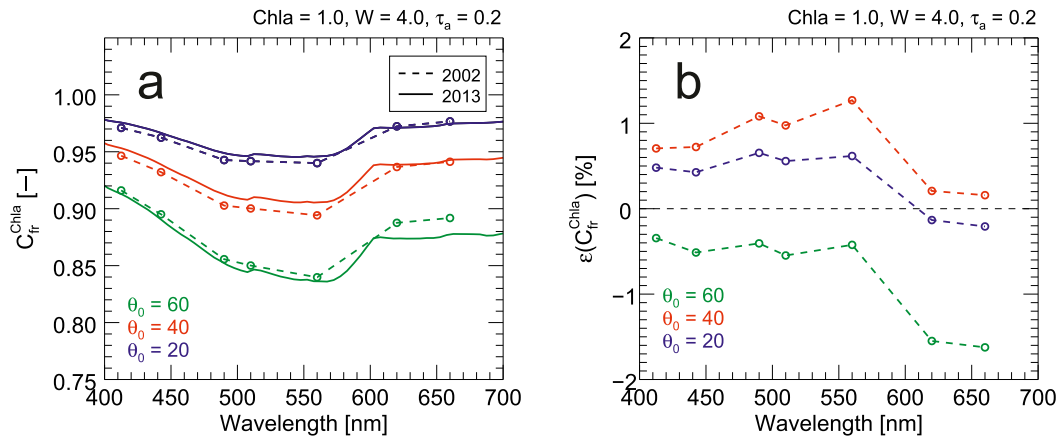


FIG. 4. (a) Correction factors C_{fr}^{Chla} determined from the f/Q -2002 and f/Q -2013 lookup tables with parameters $\theta = 40^\circ$, $\varphi = 90^\circ$, $W = 4 \text{ m s}^{-1}$, $Chla = 1 \text{ mg m}^{-3}$, $\tau_a = 0.2$, and $\theta_0 = [20^\circ, 40^\circ, 60^\circ]$, and (b) the related percent differences ε between C_{fr}^{Chla} determined from the f/Q -2013 and f/Q -2002 values.

490, 510, 560, 620, and 660 nm), and consequently do not confidently support corrections for bidirectional effects at significantly different center wavelengths. Because of this, new lookup tables (hereinafter identified as f/Q -2013) produced by the Observatoire Océanologique de Villefranche-sur-Mer applying the same processing solutions as in Morel et al. (2002), but with a spectral resolution of 5 nm and extending over the 350–700 nm spectral range (B. Gentili, unpublished data), have now been incorporated in the current AERONET-OC processing. The f/Q -2013 lookup tables with higher spectral resolution and spectral range relative to f/Q -2002, provide the immediate advantage to allow determining the correction factors C_{fr} for the Chla-based approach minimizing uncertainties due to spectral extrapolations. Further advantage offered by the f/Q -2013 with respect to the f/Q -2002 tables is the possibility of indexing the clear sky illumination conditions as a function of τ_a with values of 0.05, 0.10, 0.2, 0.4, and 1.0.

As already anticipated, an additional implementation incorporated in the current AERONET-OC processing supporting the version-3 database is the IOP-based correction approach to generate $L_{WN}(\lambda)$ likely free from the water type restrictions intrinsic of the Chla-based one.

A brief introduction to both the Chla- and IOP-based correction approaches is provided in the following subsections, while an evaluation of their impact on AERONET-OC data representativity of different water types is addressed in the discussion section.

1) CHLA-BASED CORRECTION APPROACH

The Chla-based approach minimizes the dependence of $L_W(\theta, \varphi, \lambda)$ on the viewing geometry and solar zenith following Eq. (2) with $C_{fr}(\theta, \varphi, \theta_0, \lambda, \tau_a, \text{IOP}, W)$ given by

$$C_{fr}^{Chla}(\theta, \varphi, \theta_0, \lambda, \tau_a, \text{IOP}, W) = \frac{\Re(0, W) Q(\theta, \varphi, \theta_0, \lambda, \tau_a, \text{Chla})}{\Re(\theta, W) f(\theta_0, \lambda, \tau_a, \text{Chla})} \times \frac{f(0, \lambda, \tau_a, \text{Chla})}{Q(0, 0, 0, \lambda, \tau_a, \text{Chla})} \quad (3)$$

where \Re accounts for combined reflection/refraction effects on the downward irradiance and upwelling radiance propagating through the water surface, Q is the Q factor indicating the ratio of upward irradiance to upwelling radiance just below the surface, and f relates the irradiance reflectance to the water IOPs. The aerosol optical depth τ_a expresses dependence on the atmospheric optical properties and the chlorophyll- a concentration $Chla$ indicates dependence on IOPs. It is recalled that the values of $Chla$ applied for the determination of C_{fr}^{Chla} and accessible in both the version-2 and version-3 databases, are computed through band-ratio algorithms (Zibordi et al. 2009b). When available, as for the Adriatic, Baltic and Black Sea sites (see Zibordi et al. 2009a, 2015), regional algorithms are applied. Conversely, the OC2v4 algorithm (O'Reilly et al. 2000) developed relying on a global dataset representative of both oligotrophic and eutrophic waters, is used. Because of this, AERONET-OC $Chla$ values need to be considered best estimates with uncertainties that may largely vary across sites.

With reference to Morel et al. (2002), by assuming Case-1 waters, simulated values of \Re and f/Q included in the f/Q -2002 and f/Q -2013 tables were determined as a function of the relevant variables. Taking into account the different f/Q values, Fig. 4 shows a basic comparison of the correction factors C_{fr}^{Chla} extracted from the f/Q -2002 and f/Q -2013 lookup tables. The analysis is restricted to the AERONET-OC viewing geometry (i.e., $\theta = 40^\circ$, $\varphi = 90^\circ$) with $W = 4 \text{ m s}^{-1}$, $Chla = 1 \text{ mg m}^{-3}$, $\tau_a = 0.2$ and various solar zenith angles (i.e., $\theta_0 = [20^\circ, 40^\circ, 60^\circ]$). Results indicate a close agreement between C_{fr}^{Chla} from the f/Q -2002 and f/Q -2013 table values. Still, differences exhibit an impact that may slightly exceed $\pm 1\%$ in $L_{WN}(\lambda)$ for the specific case considered.

2) IOP-BASED CORRECTION APPROACH

The IOP-based approach (Lee et al. 2011) relies on the application of the following equation relating $L_W(\theta, \varphi, \lambda)$ to the inherent optical properties:

$$L_W(\theta, \varphi, \lambda) = E_d(\lambda) \left[G_0^w(\theta, \varphi, \theta_0) + G_1^w(\theta, \varphi, \theta_0) \frac{b_{bw}(\lambda)}{a(\lambda) + b_b(\lambda)} \right] \times \frac{b_{bw}(\lambda)}{a(\lambda) + b_b(\lambda)} + \left[G_0^p(\theta, \varphi, \theta_0) + G_1^p(\theta, \varphi, \theta_0) \frac{b_{bp}(\lambda)}{a(\lambda) + b_b(\lambda)} \right] \frac{b_{bp}(\lambda)}{a(\lambda) + b_b(\lambda)}, \quad (4)$$

where $E_d(\lambda)$ is the downward irradiance. The symbol $a(\lambda)$ indicates the water absorption coefficient defined by the contributions of pure seawater $a_w(\lambda)$, detritus plus CDOM $a_{dg}(\lambda)$ and phytoplankton $a_{ph}(\lambda)$. The symbol $b_b(\lambda)$ indicates the water backscattering coefficient given by the sum of the contributions of water molecules $b_{bw}(\lambda)$ and particles $b_{bp}(\lambda)$.

The approach implies the determination of $a(\lambda)$ and $b_b(\lambda)$ from Eq. (4) using the model coefficients $G_0^w(\theta, \varphi, \theta_0)$, $G_1^w(\theta, \varphi, \theta_0)$, $G_0^p(\theta, \varphi, \theta_0)$ and $G_1^p(\theta, \varphi, \theta_0)$ derived from simulated $L_W(\theta, \varphi, \lambda)$. From the retrieved values of $a(\lambda)$ and $b_b(\lambda)$, $L_{WN}(\lambda)$ is then determined using the model coefficients $G_0^w(0, 0, 0)$, $G_1^w(0, 0, 0)$, $G_0^p(0, 0, 0)$ and $G_1^p(0, 0, 0)$ in agreement with

$$L_{WN}(\lambda) = E_0(\lambda) \left[G_0^w(0, 0, 0) + G_1^w(0, 0, 0) \frac{b_{bw}(\lambda)}{a(\lambda) + b_b(\lambda)} \right] \frac{b_{bw}(\lambda)}{a(\lambda) + b_b(\lambda)} + \left[G_0^p(0, 0, 0) + G_1^p(0, 0, 0) \frac{b_{bp}(\lambda)}{a(\lambda) + b_b(\lambda)} \right] \frac{b_{bp}(\lambda)}{a(\lambda) + b_b(\lambda)}, \quad (5)$$

where $E_0(\lambda)$ is the mean extra-atmospheric solar irradiance.

d. Supervised spectrum-by-spectrum quality check

The supervised spectrum-by-spectrum quality check introduced in section 2 aims at creating a list of flagged $L_{WN}(\lambda)$ spectra. Drawback of such a solution is the relative time-consuming process and the potential for subjective decisions on dubious cases. Still, the process is fundamental to quality check $L_{WN}(\lambda)$ data from unique water types or related to occasional biological events, that could be rejected by an automatic scheme based on statistical methods.

A graphical user interface (GUI) supports the supervised spectrum-by-spectrum quality check of $L_{WN}(\lambda)$ prior being qualified for level 2.0 through a number of synoptic verifications. A snapshot of the GUI is presented in Fig. 5 to illustrate its various components identified as (i) reduced dimension spectral mapping (latent maps), (ii) spectral self-consistency, (iii) spectral time consistency, (iv) temporal evolution, and (v) additional details.

The comprehensive specifics provided by these verifications should allow any experienced analyst to decide on the quality of each spectrum candidate to level 2.0. Decisions are saved in an *exclusion list* containing details on the $L_{WN}(\lambda)$ spectra to be excluded from level 2.0. It is, however, anticipated that an effort is ongoing to automatize most of the current quality assurance/control scheme.

With reference to Fig. 5 the various elements of this final quality check based on decisions from an experienced analyst are briefly summarized:

- 1) Reduced dimension spectral mapping (latent maps, column 1 in Fig. 5) aims at verifying the pertinence of the $L_{WN}(\lambda)$ spectrum to a specific water type (i.e., chlorophyll-*a*-, CDOM-, or non-CDOM-dominated optically complex waters) and its statistical representativity in the AERONET-OC dataset going to be screened. This is achieved by projecting the $L_{WN}(\lambda)$ spectrum to be

examined on a latent map obtained with reference $L_{WN}(\lambda)$ data whose accuracy and water type membership are known (D'Alimonte et al. 2012; Zibordi et al. 2011). The axes of the reference latent maps are the first two components from principal component analysis (PCA) applied to $L_{WN}(\lambda)/L_{WN}(560)$ normalized reference spectra (upper map) and $L_{WN}(560)$ versus the first PCA component (lower map). This step is completed by projecting N additional AERONET-OC $L_{WN}(\lambda)$ spectra exhibiting PCA and $L_{WN}(560)$ features equivalent to that of the examined spectrum (here $N = 25$). The radius of the circle enclosing the previous spectra (i.e., the examined one and the additional N) in the map displaying the first two PCA components, provides qualitative indication on the actual statistical representativity of the shape of the examined spectrum into the dataset: a larger circle indicates a spectrum exhibiting a lower statistical representativity in the dataset to be screened. Overall the latent maps are most beneficial for newly established sites for which the water type needs to be identified or alternatively for sites exhibiting a variety of water types.

- 2) Spectral self-consistency (column 2 in Fig. 5) aims at providing a physical visualization of the examined spectrum (displayed in blue) and of the additional N exhibiting similar features in the latent space. The $L_{WN}(\lambda)$ spectra are displayed both in absolute units and normalized values. The graphs aim at further assist with the assessment of the spectral consistency of the examined spectrum with respect to those having similar features in the latent maps.
- 3) Spectral time consistency (column 3 in Fig. 5) aims at showing the examined spectrum (displayed in blue) in conjunction with all those pertaining to a specific time interval ΔT (here $\Delta T = 12$ h). In this case, the graphs displaying the absolute and normalized spectra, provide means to compare the spectrum to be examined with those occurring close in time and expected to likely show similar

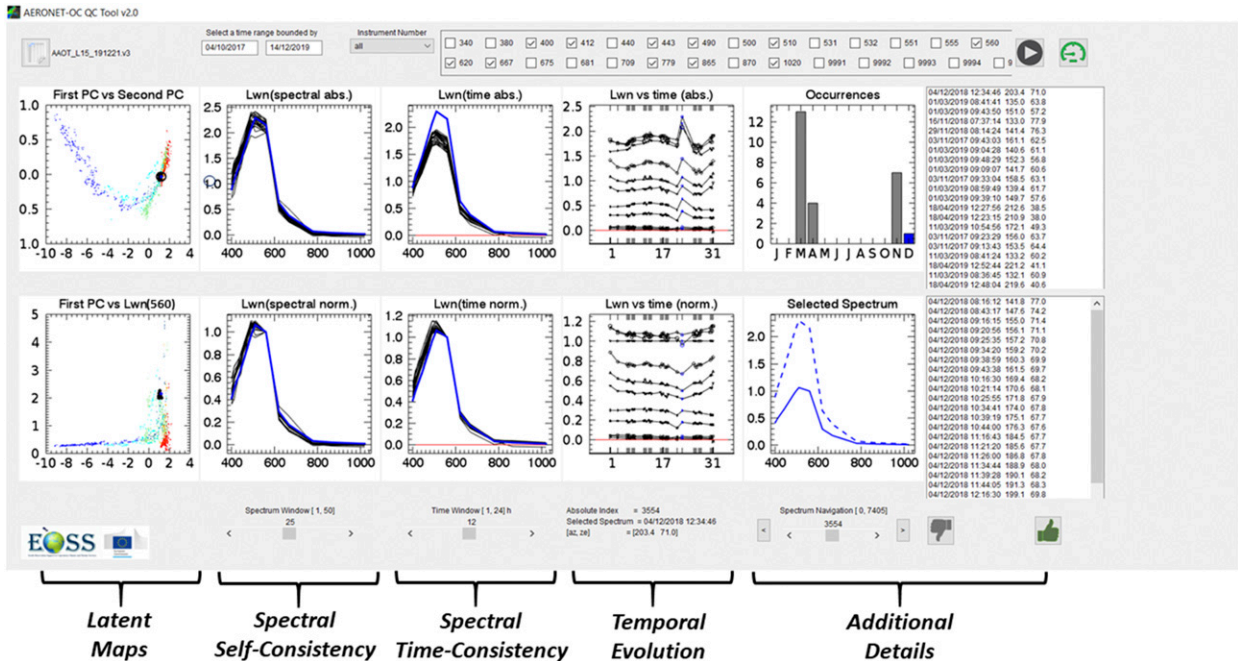


FIG. 5. Snapshot of the GUI supporting the supervised spectrum-by-spectrum quality check of $L_{WN}(\lambda)$ data. The blue color is used to highlight the examined spectrum.

spectral features. The example provided in the snapshot shows the examined spectrum exhibiting anomalously high absolute values at 490nm and at 560nm likely due to surface perturbations (e.g., glint, foam, floating material). It is mentioned that the red horizontal lines aim at highlighting any negative value of the examined spectrum.

4) Temporal evolution (column 4 in Fig. 5) aiming at providing the actual temporal representation of each spectrum displayed in the spectral time-consistency graphs. These plots, which also display the spectral data in absolute units and normalized values (which implies a constant value of 1 at 560 nm for all the normalized spectra), are designed to help determining if any temporal change can be explained by the dynamic of the site. Actually, the spectrum showing anomalously high absolute values in the spectral time-consistency graph, is responsible for an abrupt change with time in the temporal

evolution plots: this supports the hypothesis of occasional surface perturbations affecting $L_T(\theta, \varphi, \lambda)$ data.

5) Additional details (columns 5 and 6 in Fig. 5) provided by the GUI include a graphical representation of the month of relevance for the examined spectrum (displayed in blue) with respect to the overall temporal distribution of the data to be screened; an individual representation in absolute units and normalized values of the examined spectrum; and finally the lists of the spectra contributing to spectral self-consistency (upper list) and spectral time consistency (lower list) with information on date, time, solar zenith and azimuth angles.

4. Discussion

From 2002 up to now, AERONET has shown an increase of one order of magnitude of $L_{WN}(\lambda)$ data at the various quality levels (see Fig. 6) accompanied by an equivalent

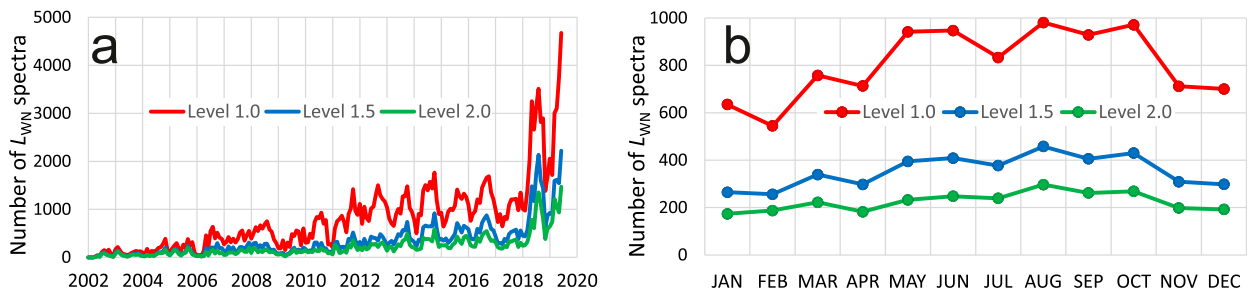


FIG. 6. (a) Number of AERONET-OC L_{WN} spectra at level 1.0, level 1.5, and level 2.0 determined for the period from 2002 until mid-2019 for which $L_{WN}(\lambda)$ have been available at all quality levels for the major sites, and (b) monthly means of the number of AERONET-OC L_{WN} spectra across the same period with seasonal variations explained by the majority of current sites operated in the Northern Hemisphere.

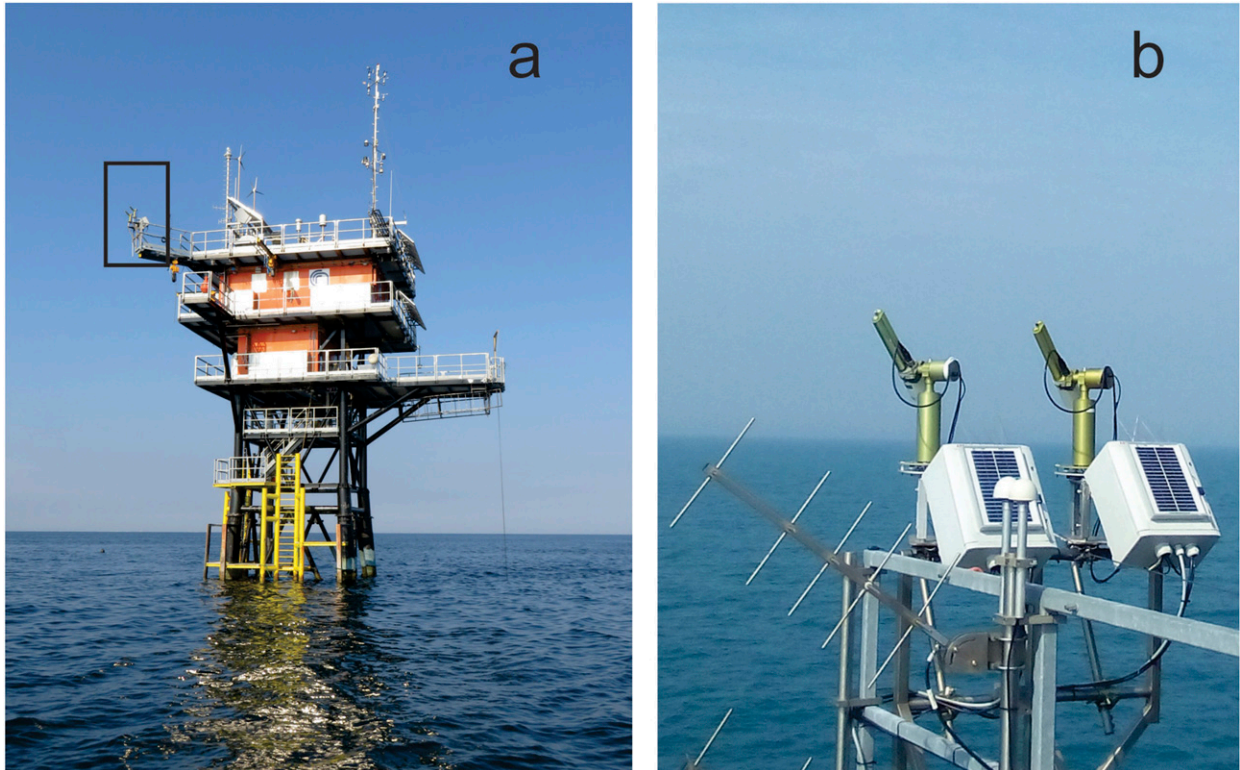


FIG. 7. (a) AAOT, and (b) detail of the deployment jetty hosting the CE-318 and CE-318T collocated radiometer systems operated to verify the equivalence of their performance.

growth of data users. The discussion section is thus devoted to those elements relevant for AERONET-OC data applications. These embrace a verification of the equivalent performance of CE-318 and CE-318T systems, the representativity of sample AERONET-OC sites across various marine regions, and finally the impact of the Chla- and IOP-based correction approaches on $L_{WN}(\lambda)$ across AERONET-OC sites.

a. Equivalence of performance between radiometer series

An extended comparison of CE-318 and CE-318T derived $L_W(\theta, \varphi, \lambda)$ and $L_{WN}(\lambda)$ data products was performed by operating collocated systems deployed at the AAOT on a jetty extending beyond the upper floor of the main structure (see Fig. 7).

The comparison has been restricted to data from instruments deployed during November 2017–July 2018 and August 2019–September 2020. Data from an intermediate deployment have been excluded due to a significant bias affecting the radiance measurements from the CE-318, not explained by the pre- and postdeployment calibrations. The proposed comparison benefits from 753 matchups constructed from CE-318 and CE-318T quality-checked measurement sequences performed within 5 min from each other. The relevant quantities defining the measurement conditions [i.e., W , θ_0 , $\tau_a(560)$, and Chla] are provided in Fig. 8 in the form of distributions. To be noted, the values of wind speed exhibit median $m = 2.54 \text{ m s}^{-1}$ and

standard deviation $\sigma = 1.63 \text{ m s}^{-1}$, which indicate that the comparison is restricted to relatively low-to-mild sea states (common to AERONET-OC data due to the glint filtering embedded in the quality assurance process). The values of θ_0 vary from approximately 20° to 80° with median $m = 43.1^\circ$, $\tau_a(560)$ exhibits median $m = 0.13$ and standard deviation $\sigma = 0.10$, and Chla estimated with a regional bio-optical algorithm (Berthon and Zibordi 2004) shows median $m = 0.95 \text{ mg m}^{-3}$ and standard deviation $\sigma = 0.94 \text{ mg m}^{-3}$.

Comparison results are provided in Fig. 9 for both $L_W(\theta, \varphi, \lambda)$ and $L_{WN}(\lambda)$, restricted to equivalent center wavelengths. It is mentioned that the impact of differences in center wavelengths (e.g., 551 nm for CE-318 data and 560 nm for CE-318T) has been minimized through the application of band-shift corrections to the CE-318 data (Zibordi et al. 2009a). Results show $L_W(\theta, \varphi, \lambda)$ from CE-318T with respect to those from CE-318, exhibiting a spectrally averaged median of percent differences $\psi_m = -0.45\%$ and a spectrally averaged median of absolute differences $|\psi|_m = 2.95\%$. The corresponding statistical values for $L_{WN}(\lambda)$ show very close values (i.e., $\psi_m = -0.04\%$ and $|\psi|_m = 2.60\%$) indicating a minor impact by the normalization process.

Spectral results from the $L_{WN}(\lambda)$ comparison are summarized in Table 5 for the equivalent center wavelengths. The value of ψ_m spectrally varies between approximately 0% and -2% while $|\psi|_m$ is generally within 3% in the blue–green spectral region but approaches 5% at 667 nm. The latter higher

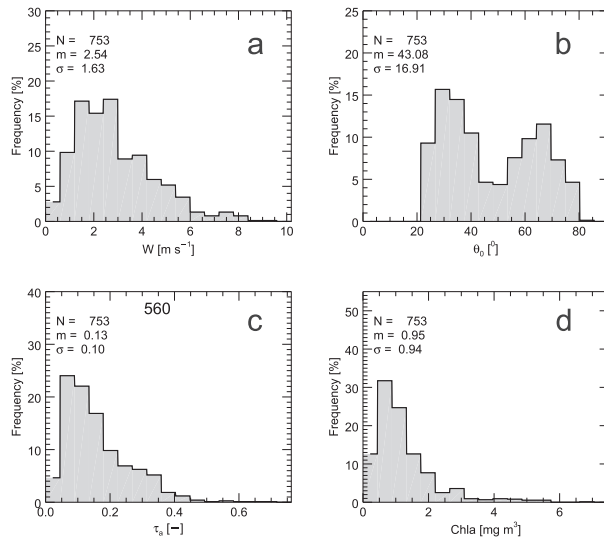


FIG. 8. Frequency distribution of (a) W , (b) θ_0 , (c) τ_a at 560 nm, and (d) Chla characterizing the AAOT $L_{WN}(\lambda)$ applied for the comparison of the CE-318 and CE-318T radiometer systems. The symbol N indicates the number of matchups, m is the median, and σ is the standard deviation of the considered quantities.

dispersion value in the red with respect to those in the blue–green spectral regions is explained by environmental perturbations enhanced by the very low radiance values characterizing $L_{WN}(\lambda)$ at 667 nm. Overall, the above differences are explained by the combined uncertainties affecting $L_{WN}(\lambda)$ AERONET-OC data assumed identical for both CE-318 and CE-318T products.

Figure 10 displays the scatterplots of the standard deviations $\sigma(L_T)$ at the sample center wavelengths 490 and 667 nm for the CE-318 and CE-318T quality assured sequences of the N_T sea-radiance measurements leading to the determination of $L_T(\theta, \varphi, \lambda)$. The similarity of $\sigma(L_T)$ for the data from the

two systems indicates equivalent wave effects in the independent determinations of $L_T(\theta, \varphi, \lambda)$. In fact, the lack of large systematic differences in $\sigma(L_T)$ suggests equivalent wave perturbations in sea-viewing measurements from the two radiometer systems. Remember that the relatively small $\sigma(L_T)$ is the result of the application of the glint filtering to measurement sequences during the quality assurance process (see section 2). Note that the large dispersion of the plotted $\sigma(L_T)$ values is explained by the random nature of wave perturbations characterizing the independent CE-318 and CE-318T measurements.

These findings support the temporal consistency of the accuracy of AERONET-OC data at and across sites regardless of the instrument operated (i.e., CE-318 or CE-318T). Still, an analysis performed on the standard deviation $\sigma(L_i)$ of the N_i sky-radiance measurements leading to the determination of $L_i(\theta', \varphi, \lambda)$ for collocated CE-318 and CE-318T systems, has shown occasional higher values of $\sigma(L_i)$ for CE-318T than for CE-318 measurements. These higher values of $\sigma(L_i)$ are likely explained by instrumental noise and are currently under investigation. This noise may occasionally prevent raising to level 2.0 the $L_{WN}(\lambda)$ retrieved from CE-318T measurements when $\sigma(L_i)$ exceeds the thresholds permitted (see section 3).

b. Representativity of sites across water types

AERONET-OC $L_{WN}(\lambda)$ spectra from different sites exhibit features representative for various water types. Data from sample sites are displayed in Fig. 11. The different panels show spectra from Casablanca Platform (CPL) in the western Mediterranean Sea frequently characterized by chlorophyll-*a*-dominated waters, the AAOT in the northern Adriatic Sea characterized by moderately sediment-dominated waters, Gloria (GLR) in the northwestern Black Sea characterized by waters dominated by sediments and CDOM, and finally Gustaf Dalen Lighthouse (GDLT) exhibiting waters heavily dominated by CDOM.

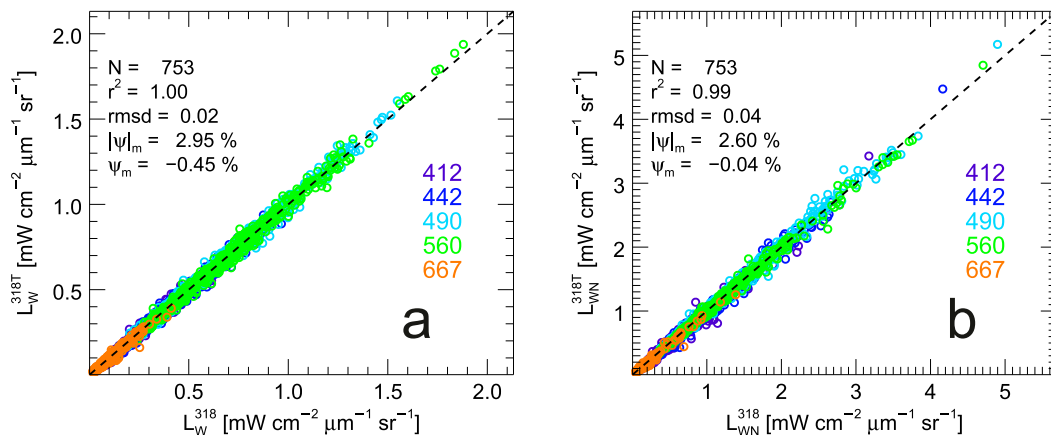


FIG. 9. Scatterplots of (a) $L_W(\theta, \varphi, \lambda)$ and (b) $L_{WN}(\lambda)$ at matching center wavelengths (nm) from collocated CE-318T and CE-318 deployed at the AAOT. The symbol N indicates the number of matchups, r^2 is the determination coefficient, rmsd is the root-mean-square deviation, $|\psi|_m$ is the spectrally averaged median of absolute percent differences, and ψ_m is the spectrally averaged median of percent differences, both of the latter determined with respect to CE-318T data.

TABLE 5. Statistical results from the spectral comparison of $L_{\text{WN}}(\lambda)$ from CE-318T and CE-318 radiometers at corresponding center wavelengths in the 412–667-nm spectral interval for the 753 matchups analyzed. The symbol ψ_m indicates the median of percent spectral differences, and $|\psi|_m$ is the median of absolute percent spectral differences [both with respect to the CE-318 $L_{\text{WN}}(\lambda)$ data]. The symbol Δ_m indicates the median of spectral differences, $|\Delta|_m$ is the median of absolute spectral differences, rmsd is the root-mean-square deviation (all in units of $\text{mW cm}^{-2} \mu\text{m}^{-1} \text{sr}^{-1}$), and r^2 is the determination coefficient.

	412	442	490	560	667
ψ_m	-0.97	-0.33	+1.44	+0.04	-2.14
$ \psi _m$	3.09	2.32	2.10	1.97	4.83
Δ_m	0.02	0.02	0.02	0.02	0.01
$ \Delta _m$	-0.01	-0.00	+0.01	-0.00	-0.00
rmsd	0.05	0.05	0.05	0.04	0.02
r^2	0.98	0.99	0.99	0.99	0.98

The actual representativity of the $L_{\text{WN}}(\lambda)$ spectra from the previous sites with respect to those from a wide range of water types included in the Bio-Optical Mapping of Marine Properties (BiOMaP) dataset (Zibordi et al. 2011), is illustrated through the latent maps displayed in Fig. 12 featuring the shape and amplitude of spectra (D'Alimonte et al. 2012). Specifically, as already detailed in section 3, the $L_{\text{WN}}(\lambda)$ spectral shape is presented through the first two PCA components determined for the spectra normalized to their value at 560 nm (i.e., $L_{\text{WN}}(\lambda)/L_{\text{WN}}(560)$) while the amplitude is simply determined by the $L_{\text{WN}}(560)$ value.

With reference to Fig. 12, the circles indicate the projection of the BiOMaP $L_{\text{WN}}(\lambda)$ spectra classified applying a priori knowledge on their nature: oligotrophic and mesotrophic chlorophyll-*a*-dominated waters in blue, CDOM-dominated waters in red, and any other optically complex water in green. The contour plots designate the density distribution of the AERONET-OC projected $L_{\text{WN}}(\lambda)$ spectra. Specifically, the

AERONET-OC projected spectra are mapped to a uniform grid where the number of occurrences at each grid element determines the contour lines.

Interestingly, as anticipated by the shape of the mean spectra displayed in Fig. 11, the AERONET-OC $L_{\text{WN}}(\lambda)$ spectra projected in Fig. 12 confirm ample representativity for the various water types with respect to the BiOMaP dataset. In summary, the above analysis supports the exploitation of AERONET-OC $L_{\text{WN}}(\lambda)$ in validation activities across a variety of water types such as chlorophyll-*a*-dominated waters at CPL, highly CDOM-dominated waters at GDLT, and finally waters dominated by different concentrations of sediments and CDOM at AAOT and GLR.

c. Impact of Chla- and IOP-based corrections for bidirectional effects

The impact of Chla- and IOP-based corrections for bidirectional effects are discussed by comparing $L_{\text{WN}}(\lambda)$ obtained with the two correction approaches. Before addressing results from the comparison, it is reminded that the Cha approach was conceived for Case-1 waters: consequently, its application to optically complex waters may become the source of large uncertainties. Still, the Chla approach is applied to AERONET-OC data as well as to satellite ocean color radiometric products from various missions. Because of this, the comparison of the two different correction approaches using AERONET-OC data from a variety of water types is of relevance for the user community.

An additional element requiring clarification is the application of both $C_{\text{fr}}^{\text{Chla}}$ and $C_{\text{fr}}^{\text{IOP}}$ up to the 667-nm center wavelength for marine and up to 709 nm for lake data. Thus, corrections $C_{\text{fr}}^{\text{Chla}}$ and $C_{\text{fr}}^{\text{IOP}}$ are not applied to $L_{\text{W}}(\theta, \varphi, \lambda)$ data at center wavelengths beyond 709 nm for which the uncertainties are expected to exceed several tens of percent.

Results from comparisons performed for AERONET-OC representative sites (i.e., CPL, AAOT, GLR and GDLT) are

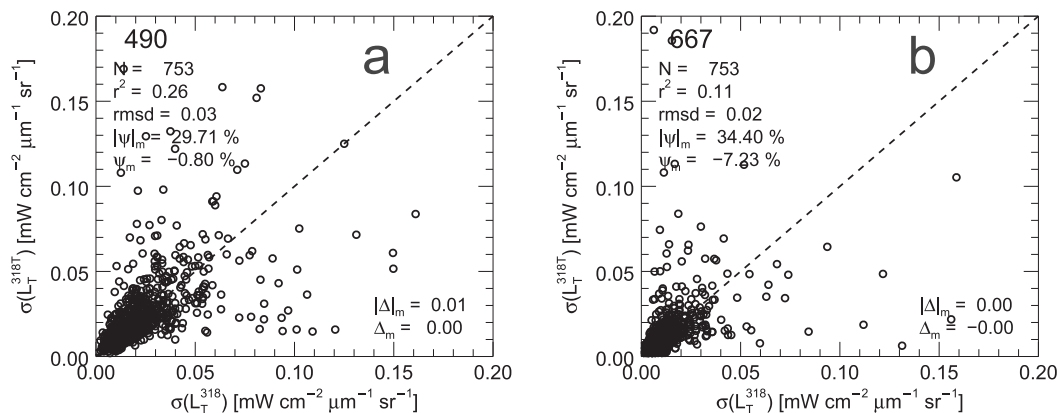


FIG. 10. Scatterplots of the standard deviations $\sigma(L_T)$ [indicating either $\sigma(L_T^{318})$ and $\sigma(L_T^{318T})$] at the (a) 490- and (b) 667-nm center wavelengths for the CE-318T and CE-318 measurement sequences contributing to the comparison of systems performance. The symbol N indicates the number of matchups, r^2 is the determination coefficient, rmsd is the root-mean-square deviation, $|\psi|_m$ is the median of absolute percent differences, ψ_m is the median of percent differences, $|\Delta|_m$ is the median of absolute differences, and Δ_m is the median of differences.

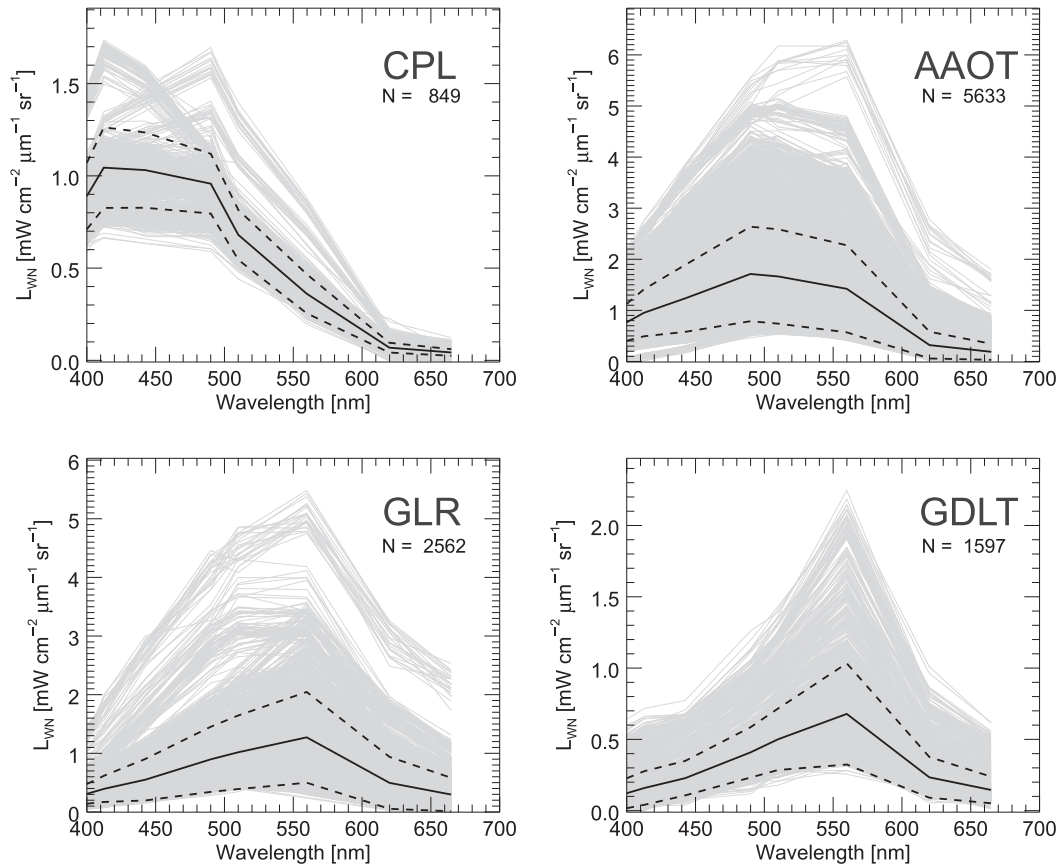


FIG. 11. AERONET-OC level 2.0 $L_{WN}(\lambda)$ spectra from the CPL, AAOT, GLR, and GDLT sites (corrected through the Chla approach). The thick black line indicates mean values, and the thick dashed lines indicate $\pm 1\sigma$; N indicates the number of spectra.

summarized in Fig. 13 through scatterplots of $L_{WN}^{IOP}(\lambda)$ versus $L_{WN}^{Chla}(\lambda)$ to illustrate the relative spectrally averaged impact of the two corrections, and additionally with graphs showing the mean and related standard deviation of the spectral corrections (i.e., C_{fr}^{Chla} and C_{fr}^{IOP} for the Chla- and IOP-based approaches, respectively).

As expected, both the scatterplots and the graphs displaying corrections indicate relatively low absolute differences between methods for CPL characterized by Case-1 waters. In this specific case, notable is the small spectral dependence of both corrections.

A higher disagreement between C_{fr}^{Chla} and C_{fr}^{IOP} values is shown for AAOT, GLR and GDLT, all characterized by optically complex waters. Regardless of the relatively small spectrally averaged values of ψ_m , which are all within approximately $\pm 2\%$ and consequently suggest minor biases between the $L_{WN}^{IOP}(\lambda)$ and $L_{WN}^{Chla}(\lambda)$ data products, C_{fr}^{IOP} and C_{fr}^{Chla} exhibit marked spectral differences approaching mean values of $\pm 5\%$. Notable is the higher spectral dependence of C_{fr}^{Chla} with respect to C_{fr}^{IOP} with corrections that may exceed -15% at 560 nm for C_{fr}^{Chla} versus approximately -10% for C_{fr}^{IOP} (see the panels referring to GLR and GDLT in Fig. 13). This difference varies with the solar zenith angle and thus exhibits a seasonal dependence. Evidence is provided in Fig. 14 at the 490 and

667 nm center wavelengths for the CPL and AAOT sites, respectively, representative for chlorophyll-*a*-dominated and optically complex waters.

We also mention that both the Chla- and IOP-based correction approaches are sensitive to the spectral values of extra-atmospheric solar irradiance $E_0(\lambda)$. For the Chla-based approach the impact on $L_{WN}(\lambda)$ comes from the determination of Chla through band-ratio algorithms relying on the remote sensing reflectance $R_{RS}(\lambda)$ [where $R_{RS}(\lambda) = L_{WN}(\lambda)/E_0(\lambda)$]. In the specific case of the version-2 and version-3 databases, applying the ASTM E490 (Tobiska 2002) and NRL SSI2 (Coddington et al. 2016) $E_0(\lambda)$, respectively, the spectral differences affecting $L_{WN}(\lambda)$ are generally lower than 0.5% across the visible spectrum. For the IOP-based approach, as a result of the application of Eq. (5), the impact is proportional to the percent difference between $E_0(\lambda)$ values, which can exceed several percent (Shanmugam and Ahn 2007).

The capability of providing $L_{WN}(\lambda)$ data independently determined applying C_{fr}^{Chla} and C_{fr}^{IOP} regardless of the water type, maximize the potentials for the exploitation of AERONET-OC data in validation exercises requiring consistent corrections for bidirectional effects in both in situ and satellite data, often varying across missions and applications.

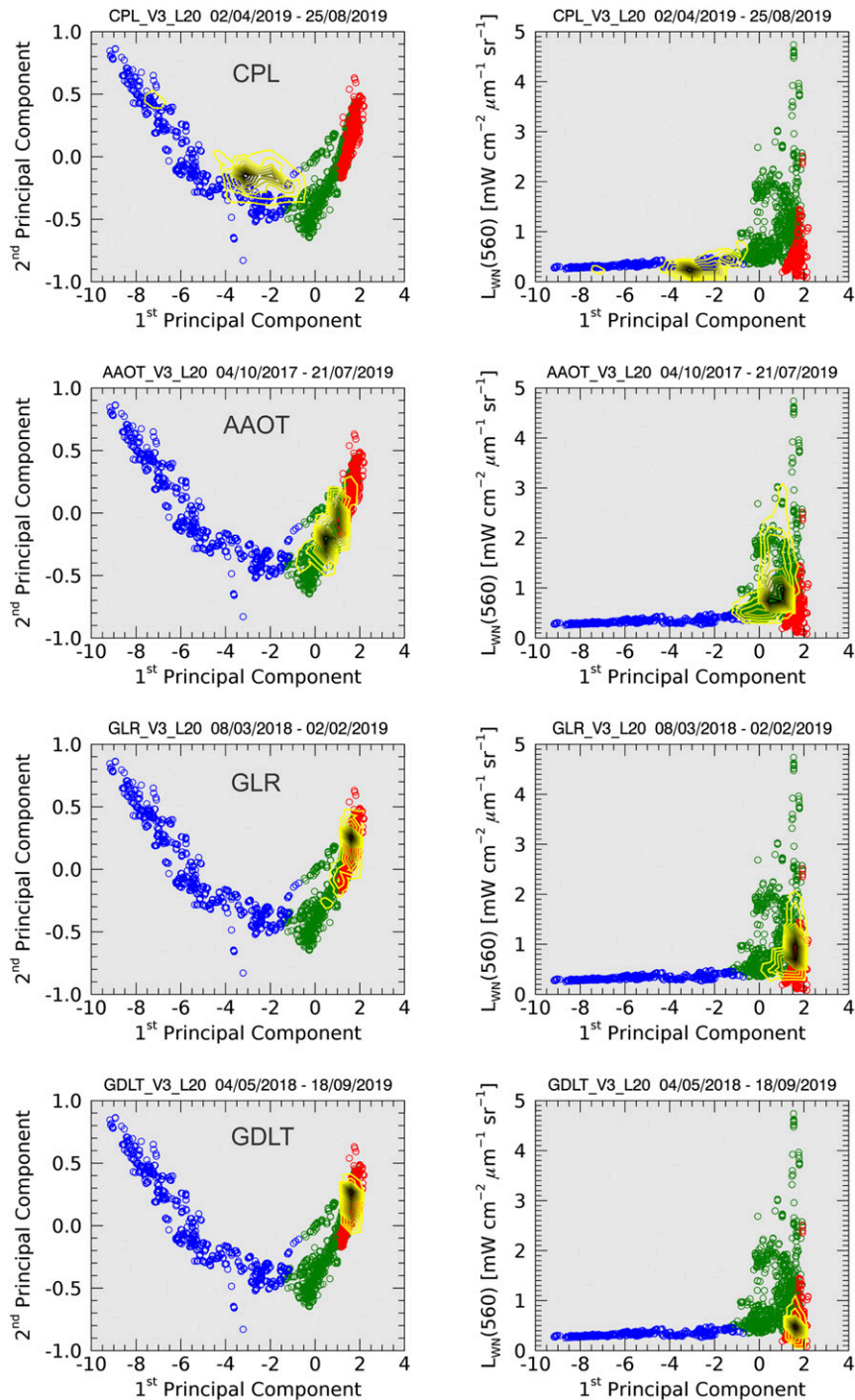


FIG. 12. Latent maps of AERONET-OC $L_{WN}(\lambda)$ spectra from (top) CPL, (top middle) AAOT, (bottom middle) GLR, and (bottom) GDLT produced with the first two PCA components applied to (left) $L_{WN}(\lambda)/L_{WN}(560)$ and (right) $L_{WN}(560)$ vs the first PCA component. The isolines, displayed at 10% increments with increasing value from light yellow to black, illustrate the density distribution of projected AERONET-OC $L_{WN}(\lambda)$ for the various AERONET-OC sites. The circles indicate the projected BiOMaP $L_{WN}(\lambda)$, with colors identifying different water types: blue for oligotrophic and mesotrophic chlorophyll-*a*-dominated waters, red for CDOM-dominated waters, and green for any other optically complex water.

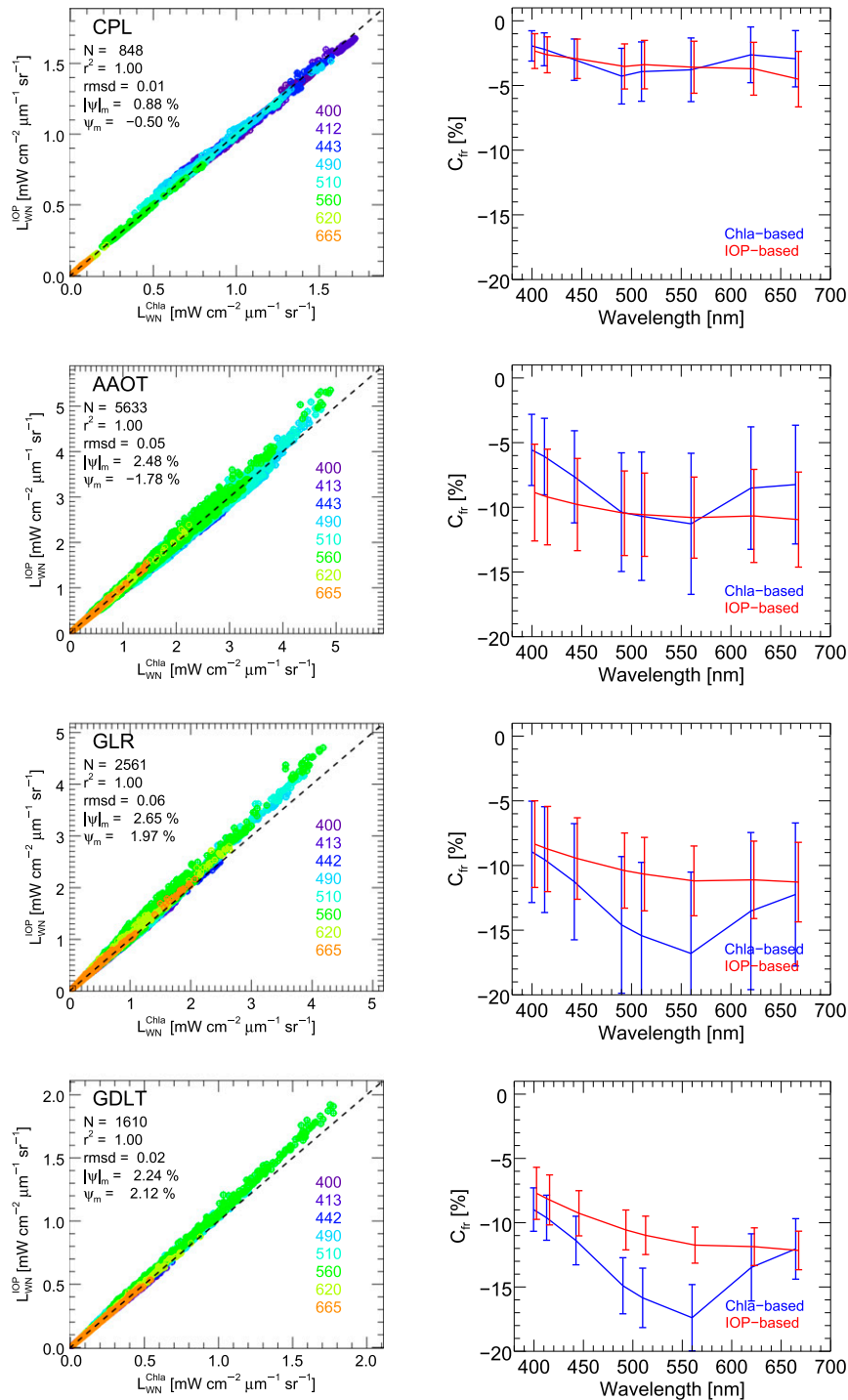


FIG. 13. (left) Scatterplots of $L_{WN}^{IOP}(\lambda)$ vs $L_{WN}^{Chla}(\lambda)$ at matching center wavelengths (nm) restricted to the visible spectral region for sample AERONET-OC sites representative of a variety of water types: CPL, AAOT, GLR, and GDLT. (right) Percent spectral corrections C_{tr} , indicating either C_{tr}^{Chla} (blue) or C_{tr}^{IOP} (red) for the various AERONET-OC sites. Symbols ψ_m and $|\psi|_m$ indicate the spectrally averaged median of percent differences and of absolute percent differences, respectively, between the corrections C_{tr}^{IOP} and C_{tr}^{Chla} , N indicates the number of spectra, $rmsd$ is the root-mean-square deviation, and r^2 is the determination coefficient.

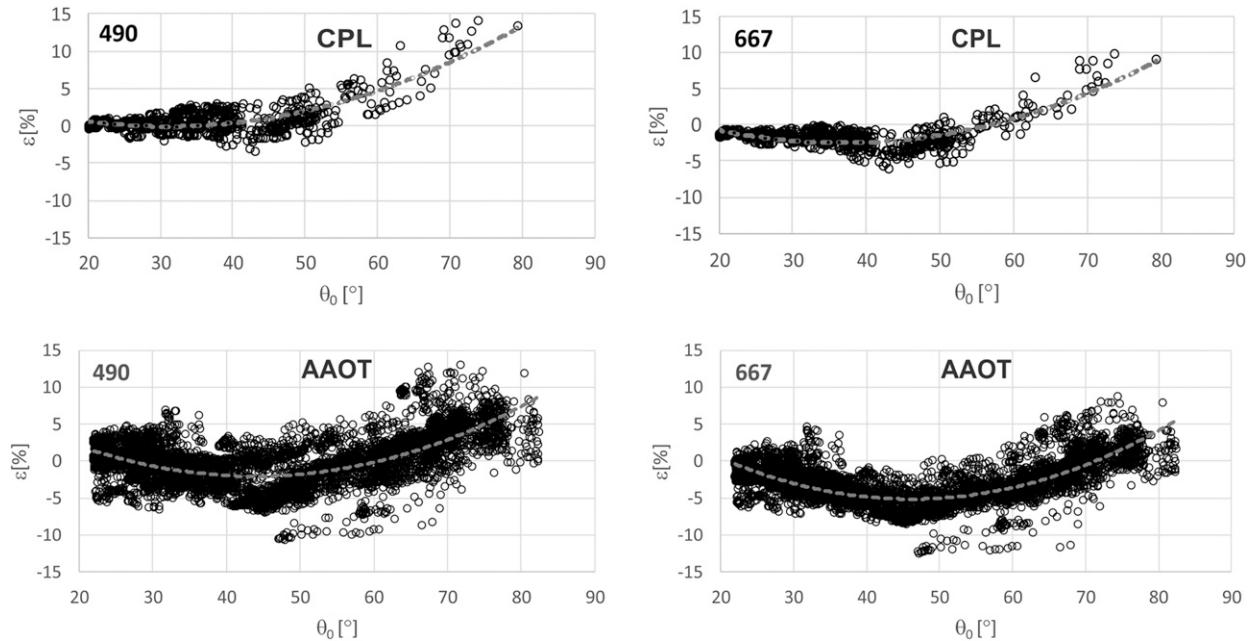


FIG. 14. Percent differences ε between $L_{\text{WN}}^{\text{IOP}}(\lambda)$ and $L_{\text{WN}}^{\text{Chla}}(\lambda)$ at the 490- and 667-nm center wavelengths as a function of θ_0 for CPL and AAOT sites. The gray dashed lines indicate the fitted values.

5. Summary and conclusions

AERONET-OC was conceived to support satellite ocean color activities through globally distributed standardized instruments operated on offshore fixed structures. After an early development phase (Zibordi et al. 2004, 2006) and successive consolidation (Zibordi et al. 2009b), AERONET-OC increased from the initial five sites constituting the network in 2006 to 31 in 2020. Concurrently, it benefitted from a number of investigations fundamental for a quantitative application of its data products. These studies further refined the quality assurance methods, addressed uncertainties across sites characterized by different water types, assessed assumptions supporting the determination of $L_{\text{WN}}(\lambda)$, verified the applicability of alternative approaches for the minimization of bidirectional effects, consolidated knowledge on the impact of spectral perturbations by deployment structures and of adjacency effects in satellite data. Additional efforts were placed in verifying and consolidating new technological advances allowing to extend the number of spectral bands from the 9 of CE-318 radiometer systems to the 12 of CE-318T ones.

This work documents recent AERONET-OC advances on hardware and data processing. Specifically, considering the transition from CE-318 to CE-318T radiometer systems, the work provides evidence of the equivalence of instruments performance and data products. Additionally, after showing the variety of water types characterizing the AERONET-OC marine sites, the work illustrates differences between the Chla-based correction approach proposed for chlorophyll-*a*-dominated waters and the IOP-based one expected to be applicable to both chlorophyll-*a*-dominated and optically complex waters. Comparable corrections for bidirectional effects are shown by the two approaches at a site characterized

by oligotrophic-mesotrophic chlorophyll-*a*-dominated waters. As expected, corrections exhibit (absolute) differences exceeding several percent with a pronounced spectral dependence for optically complex waters.

Note also that the AERONET-OC version-3 database includes $L_{\text{WN}}(\lambda)$ from either CE-318 9-channel and CE-318T 12-channel radiometer systems corrected for bidirectional effects applying both the Chla- and IOP-based approaches regardless of the water type. This solution aims at ensuring the widest support to the application of AERONET-OC data in matchup analysis for satellite data products from various missions.

Acknowledgments. Acknowledgments are given to the entire AERONET team for the effort to include and sustain the ocean color component in the AERONET observational network. Extensive acknowledgments are also given to Bernard Gentili from the Observatoire Océanologique de Villefranche-sur-Mer (France) for providing access to the updated version of the f/Q tables. Acknowledgments are given to Tamito Kajiyama for assisting with the programming of the routines required for the IOP-based corrections.

Data availability statement. AERONET-OC data are available from NASA (https://aeronet.gsfc.nasa.gov/new_web/ocean_color.html).

APPENDIX A

Glossary

AAOT
BiOMaP

Acqua Alta Oceanographic Tower
Bio-Optical Mapping of Marine Properties

AERONET	Aerosol Robotic Network	Q	Q factor
AERONET-OC	Ocean Color Component of AERONET	R_{RS}	Remote sensing reflectance
CDOM	Colored dissolved organic matter	\Re	Parameter defining the water surface reflection/refraction
CPL	Casablanca Platform		
DCP	Data collection platform	t_d	Diffuse atmospheric transmittance
GDLT	Gustaf Dalen Lighthouse Tower	W	Wind speed
GLR	Gloria Platform	Δ_m	Median of differences
GUM	Guide to the Expression of Uncertainty in Measurements	$ \Delta _m$	Median of absolute differences
HLT	Helsinki Lighthouse Tower	θ	Viewing angle for sea-radiance observations
GPRS	General Packet Radio Service	θ_0	Sun zenith angle
GUI	Graphical user interface	θ'	Viewing angle for sky-radiance observations
IOP	Inherent optical properties	λ	Wavelength
MODIS	Moderate Resolution Imaging Spectroradiometer	ρ	Water surface reflectance factor
OLCI	Ocean Land Color Instrument	τ_a	Aerosol optical depth
PACE	Plankton, Aerosol, Cloud and Ocean Ecosystem	$\sigma(L_i)$	Standard deviation of the N_i sky-radiance observations
PCA	Principal component analysis	$\sigma(L_T)$	Standard deviation of the N_T sea-radiance observations
SeaPRISM	SeaWiFS Photometer Revision for Incident Surface Measurements	φ	Relative azimuth between sun and sensor
SeaWiFS	Sea-Viewing Wide Field-of-View Sensor	φ_0	Sun azimuth
SD	Secure Digital	ψ	Mean of percent differences
VIIRS	Visible Infrared Imaging Radiometer Suite	$ \psi $	Mean of absolute percent differences
		ψ_m	Median of percent differences
		$ \psi _m$	Median of absolute percent differences

APPENDIX B

Primary Symbols

a	Absorption coefficient of natural water
a_{dg}	Absorption coefficient of detritus plus CDOM
a_{ph}	Absorption coefficient of phytoplankton
a_w	Absorption coefficient of pure seawater
b_b	Backscattering coefficient of natural water
b_{bp}	Backscattering coefficient of particles
b_{bw}	Backscattering coefficient of water molecules
Chl a	Chlorophyll- a concentration
C_{fr}	Correction factor for bidirectional effects
$C_{fr}^{Chl a}$	Correction factor for bidirectional effects relying on Chl a
C_{fr}^{IOP}	Correction factor for bidirectional effects relying on IOP
D	Day of the year
E	Direct sun irradiance
E_0	Extra-atmospheric sun irradiance
E_d	Total downward irradiance
f	Parameter relating irradiance and IOPs
$G_0^w, G_1^w, G_0^p,$ and G_1^p	Model parameters
L_i	Sky radiance
L_T	Total radiance from the sea
L_W	Water-leaving radiance
L_{WN}	Normalized water-leaving radiance
N_i	Number of successive sky-radiance observations for the determination of L_i
N_T	Number of successive sea-radiance observations for the determination of L_T

REFERENCES

- Berthon, J.-F., and G. Zibordi, 2004: Bio-optical relationships for the northern Adriatic Sea. *Int. J. Remote Sens.*, **25**, 1527–1532, <https://doi.org/10.1080/01431160310001592544>.
- Bulgarelli, B., and G. Zibordi, 2018a: On the detectability of adjacency effects in ocean color remote sensing of mid-latitude coastal environments by SeaWiFS, MODIS-A, MERIS, OLCI, OLI and MSI. *Remote Sens. Environ.*, **209**, 423–438, <https://doi.org/10.1016/j.rse.2017.12.021>.
- , and —, 2018b: Seasonal impact of adjacency effects on ocean color radiometry at the AAOT validation site. *IEEE Geosci. Remote Sens.*, **15**, 488–492, <https://doi.org/10.1109/LGRS.2017.2781900>.
- , —, and F. Mélin, 2018: On the minimization of adjacency effects in SeaWiFS primary data products from coastal areas. *Opt. Express*, **26**, A709–A728, <https://doi.org/10.1364/OE.26.00A709>.
- Coddington, O., J. L. Lean, P. Pilewskie, M. Snow, and D. Lindholm, 2016: A solar irradiance climate data record. *Bull. Amer. Meteor. Soc.*, **97**, 1265–1282, <https://doi.org/10.1175/BAMS-D-14-00265.1>.
- Cox, C., and W. Munk, 1954: Measurement of the roughness of the sea surface from photographs of the sun's glitter. *J. Opt. Soc. Amer.*, **44**, 838–850, <https://doi.org/10.1364/JOSA.44.000838>.
- D'Alimonte, D., and G. Zibordi, 2006: Statistical assessment of radiometric measurements from autonomous systems. *IEEE Trans. Geosci. Remote Sens.*, **44**, 719–728, <https://doi.org/10.1109/TGRS.2005.862505>.
- , and T. Kajiyama, 2016: Effects of light polarization and waves slope statistics on the reflectance factor of the sea surface. *Opt. Express*, **24**, 7922–7942, <https://doi.org/10.1364/OE.24.007922>.
- , G. Zibordi, J.-F. Berthon, E. Canuti, and T. Kajiyama, 2012: Performance and applicability of bio-optical algorithms in different European seas. *Remote Sens. Environ.*, **124**, 402–412, <https://doi.org/10.1016/j.rse.2012.05.022>.
- Deschamps, P. Y., M. Herman, and D. Tanre, 1983: Modeling of the atmospheric effects and its application to the remote

- sensing of ocean color. *Appl. Opt.*, **22**, 3751–3758, <https://doi.org/10.1364/AO.22.003751>.
- Fan, Y., W. Li, C. K. Gatebe, C. Jamet, G. Zibordi, T. Schroeder, and K. Stamnes, 2017: Atmospheric correction over coastal waters using multilayer neural networks. *Remote Sens. Environ.*, **199**, 218–240, <https://doi.org/10.1016/j.rse.2017.07.016>.
- Foster, R., and A. Gilerson, 2016: Polarized transfer functions of the ocean surface for above-surface determination of the vector submarine light field. *Appl. Opt.*, **55**, 9476–9494, <https://doi.org/10.1364/AO.55.009476>.
- Gergely, M., and G. Zibordi, 2014: Assessment of AERONET-OC L_{WN} uncertainties. *Metrologia*, **51**, 40–47, <https://doi.org/10.1088/0026-1394/51/1/40>.
- Gilerson, A., C. Carrizo, R. Foster, and T. Harmel, 2018: Variability of the reflectance coefficient of skylight from the ocean surface and its implications to ocean color. *Opt. Express*, **26**, 9615–9633, <https://doi.org/10.1364/OE.26.009615>.
- Giles, D. M., and Coauthors, 2019: Advancements in the Aerosol Robotic Network (AERONET) version 3 database—Automated near-real-time quality control algorithm with improved cloud screening for sun photometer aerosol optical depth (AOD) measurements. *Atmos. Meas. Tech.*, **12**, 169–209, <https://doi.org/10.5194/amt-12-169-2019>.
- Gregg, W. W., and K. L. Carder, 1990: A simple spectral solar irradiance model for cloudless maritime atmospheres. *Limnol. Oceanogr.*, **35**, 1657–1675, <https://doi.org/10.4319/lo.1990.35.8.1657>.
- Harmel, T., A. Gilerson, A. Tonizzo, J. Chowdhary, A. Weidemann, R. Arnone, and S. Ahmed, 2012: Polarization impacts on the water-leaving radiance retrieval from above-water radiometric measurements. *Appl. Opt.*, **51**, 8324–8340, <https://doi.org/10.1364/AO.51.008324>.
- Harrison, A. W., and C. A. Coombes, 1988: An opaque cloud cover model of sky short wavelength radiance. *Sol. Energy*, **41**, 387–392, [https://doi.org/10.1016/0038-092X\(88\)90035-7](https://doi.org/10.1016/0038-092X(88)90035-7).
- Hieronimi, M., 2016: Polarized reflectance and transmittance distribution functions of the ocean surface. *Opt. Express*, **24**, A1045–A1068, <https://doi.org/10.1364/OE.24.0A1045>.
- Hlaing, S., A. Gilerson, R. Foster, M. Wang, R. Arnone, and S. Ahmed, 2014: Radiometric calibration of ocean color satellite sensors using AERONET-OC data. *Opt. Express*, **22**, 23 385–23 401, <https://doi.org/10.1364/OE.22.023385>.
- Holben, B. N., and Coauthors, 1998: AERONET—A federated instrument network and data archive for aerosol characterization. *Remote Sens. Environ.*, **66**, 1–16, [https://doi.org/10.1016/S0034-4257\(98\)00031-5](https://doi.org/10.1016/S0034-4257(98)00031-5).
- , and Coauthors, 2001: An emerging ground-based aerosol climatology: Aerosol optical depth from AERONET. *J. Geophys. Res.*, **106**, 12 067–12 097, <https://doi.org/10.1029/2001JD900014>.
- Hooker, S. B., and A. Morel, 2003: Platform and environmental effects on above-water determinations of water-leaving radiances. *J. Atmos. Oceanic Technol.*, **20**, 187–205, [https://doi.org/10.1175/1520-0426\(2003\)020<0187:PAEEOA>2.0.CO;2](https://doi.org/10.1175/1520-0426(2003)020<0187:PAEEOA>2.0.CO;2).
- , and G. Zibordi, 2005: Platform perturbations in above-water radiometry. *Appl. Opt.*, **44**, 553–567, <https://doi.org/10.1364/AO.44.000553>.
- , G. Lazin, G. Zibordi, and S. McLean, 2002: An evaluation of above- and in-water methods for determining water-leaving radiances. *J. Atmos. Oceanic Technol.*, **19**, 486–515, [https://doi.org/10.1175/1520-0426\(2002\)019<0486:AEOAAI>2.0.CO;2](https://doi.org/10.1175/1520-0426(2002)019<0486:AEOAAI>2.0.CO;2).
- IOCCG, 2019: Protocols for satellite ocean colour data validation: In situ optical radiometry. IOCCG Protocol Series Doc., 67 pp., <https://doi.org/10.25607/OBP-691>.
- Jamet, C., H. Loisel, C. P. Kuchinke, K. Ruddick, G. Zibordi, and H. Feng, 2011: Comparison of three SeaWiFS atmospheric correction algorithms for turbid waters using AERONET-OC measurements. *Remote Sens. Environ.*, **115**, 1955–1965, <https://doi.org/10.1016/j.rse.2011.03.018>.
- Johnson, B. C., G. Zibordi, S. W. Brown, M. E. Feinholz, M. G. Sorokin, I. Slutsker, J. T. Woodward, and H. W. Yoon, 2021: Characterization and absolute calibration of an AERONET-OC radiometer. *Appl. Opt.*, in press.
- Lee, Z. P., K. Du, K. J. Voss, G. Zibordi, B. Lubac, R. Arnone, and A. Weidemann, 2011: An inherent-optical-property-centered approach to correct the angular effects in water-leaving radiance. *Appl. Opt.*, **50**, 3155–3167, <https://doi.org/10.1364/AO.50.003155>.
- Mélin, F., and G. Zibordi, 2007: Optically based technique for producing merged spectra of water-leaving radiances from ocean color remote sensing. *Appl. Opt.*, **46**, 3856–3869, <https://doi.org/10.1364/AO.46.003856>.
- , and —, 2010: Vicarious calibration of satellite ocean color sensors at two coastal sites. *Appl. Opt.*, **49**, 798–810, <https://doi.org/10.1364/AO.49.000798>.
- Mobley, C. D., 1994: *Light and Water: Radiative Transfer in Natural Waters*. Academic Press, 592 pp.
- , 1999: Estimation of the remote-sensing reflectance from above-surface measurements. *Appl. Opt.*, **38**, 7442–7455, <https://doi.org/10.1364/AO.38.007442>.
- , 2015: Polarized reflectance and transmittance properties of windblown sea surfaces. *Appl. Opt.*, **54**, 4828–4849, <https://doi.org/10.1364/AO.54.004828>.
- , and L. K. Sundman, 2000: *HydroLight 4.1 User's Guide*. Sequoia Scientific, 85 pp.
- Moore, T. S., J. W. Campbell, and H. Feng, 2015: Characterizing the uncertainties in spectral remote sensing reflectance for SeaWiFS and MODIS-Aqua based on global in situ matchup data sets. *Remote Sens. Environ.*, **159**, 14–27, <https://doi.org/10.1016/j.rse.2014.11.025>.
- , and Coauthors, 2019: SeaPRISM observations in the western basin of Lake Erie in the summer of 2016. *J. Great Lakes Res.*, **45**, 547–555, <https://doi.org/10.1016/j.jglr.2018.10.008>.
- Morel, A., D. Antoine, and B. Gentili, 2002: Bidirectional reflectance of oceanic waters: Accounting for Raman emission and varying particle scattering phase function. *Appl. Opt.*, **41**, 6289–6306, <https://doi.org/10.1364/AO.41.006289>.
- O'Reilly, J. E., and Coauthors, 2000: Ocean color chlorophyll *a* algorithms for SeaWiFS, OC2, and OC4: Version 4. NASA Goddard Space Flight Center SeaWiFS postlaunch calibration and validation analyses, part 3, Rep., Vol. 11, 9–23.
- Pahlevan, N., and Coauthors, 2017: Landsat 8 remote sensing reflectance (R_{RS}) products: Evaluations, intercomparisons, and enhancements. *Remote Sens. Environ.*, **190**, 289–301, <https://doi.org/10.1016/j.rse.2016.12.030>.
- Park, Y. J., and K. Ruddick, 2005: Model of remote-sensing reflectance including bidirectional effects for case 1 and case 2 waters. *Appl. Opt.*, **44**, 1236–1249, <https://doi.org/10.1364/AO.44.001236>.
- Pitarch, J., M. Talone, G. Zibordi, and P. Groetsch, 2020: Determination of the remote-sensing reflectance from above-water measurements with the “3C model”: A further assessment. *Opt. Express*, **28**, 15 885–15 906, <https://doi.org/10.1364/OE.388683>.
- Shanmugam, P., and Y. H. Ahn, 2007: Reference solar irradiance spectra and consequences of their disparities in remote sensing of the ocean colour. *Ann. Geophys.*, **25**, 1235–1252, <https://doi.org/10.5194/angeo-25-1235-2007>.

- Smirnov, A., B. N. Holben, T. F. Eck, O. Dubovik, and I. Slutsker, 2000: Cloud-screening and quality control algorithms for the AERONET database. *Remote Sens. Environ.*, **73**, 337–349, [https://doi.org/10.1016/S0034-4257\(00\)00109-7](https://doi.org/10.1016/S0034-4257(00)00109-7).
- Talone, M., and G. Zibordi, 2019: Spectral assessment of deployment platform perturbations in above-water radiometry. *Opt. Express*, **27**, A878–A889, <https://doi.org/10.1364/OE.27.00A878>.
- , —, and Z. Lee, 2018: Correction for the non-nadir viewing geometry of AERONET-OC above water radiometry data: An estimate of uncertainties. *Opt. Express*, **26**, A541–A561, <https://doi.org/10.1364/OE.26.00A541>.
- Tan, J., R. Frouin, D. Ramon, and F. Steinmetz, 2019: On the adequacy of representing water reflectance by semi-analytical models in ocean color remote sensing. *Remote Sens.*, **11**, 2820, <https://doi.org/10.3390/rs11232820>.
- Tobiska, W. K., 2002: Variability in the solar constant from irradiances shortward of Lyman-alpha. *Adv. Space Res.*, **29**, 1969–1974, [https://doi.org/10.1016/S0273-1177\(02\)00243-0](https://doi.org/10.1016/S0273-1177(02)00243-0).
- Valente, A., and Coauthors, 2019: A compilation of global bi-optical in situ data for ocean-colour satellite applications-version two. *Earth Syst. Sci. Data*, **11**, 1037–1068, <https://doi.org/10.5194/essd-11-1037-2019>.
- Zhang, X., S. He, A. Shabani, P. W. Zhai, and K. Du, 2017: Spectral sea surface reflectance of skylight. *Opt. Express*, **25**, A1–A13, <https://doi.org/10.1364/OE.25.0000A1>.
- Zibordi, G., 2012: Comment on “Long Island Sound Coastal Observatory: Assessment of above-water radiometric measurement uncertainties using collocated multi and hyper-spectral systems.” *Appl. Opt.*, **51**, 3888–3892, <https://doi.org/10.1364/AO.51.003888>.
- , 2016: Experimental evaluation of theoretical sea surface reflectance factors relevant to above-water radiometry. *Opt. Express*, **24**, A446–A459, <https://doi.org/10.1364/OE.24.00A446>.
- , and K. J. Voss, 2014: Requirements and strategies for in situ radiometry in support of satellite ocean color. *Experimental Methods in the Physical Sciences*, Vol. 47, Academic Press, 531–556.
- , S. B. Hooker, J.-F. Berthon, and D. D’Alimonte, 2002: Autonomous above-water radiance measurements from an offshore platform: A field assessment experiment. *J. Atmos. Oceanic Technol.*, **19**, 808–819, [https://doi.org/10.1175/1520-0426\(2002\)019<0808:AAWRMF>2.0.CO;2](https://doi.org/10.1175/1520-0426(2002)019<0808:AAWRMF>2.0.CO;2).
- , F. Mélin, S. B. Hooker, D. D’Alimonte, and B. Holben, 2004: An autonomous above-water system for the validation of ocean color radiance data. *IEEE Trans. Geosci. Remote Sens.*, **42**, 401–415, <https://doi.org/10.1109/TGRS.2003.821064>.
- , and Coauthors, 2006: A network for standardized ocean color validation measurements. *Eos, Trans. Amer. Geophys. Union*, **87**, 293–297, <https://doi.org/10.1029/2006EO300001>.
- , J. F. Berthon, F. Mélin, D. D’Alimonte, and S. Kaitala, 2009a: Validation of satellite ocean color primary products at optically complex coastal sites: Northern Adriatic Sea, northern Baltic proper and Gulf of Finland. *Remote Sens. Environ.*, **113**, 2574–2591, <https://doi.org/10.1016/j.rse.2009.07.013>.
- , and Coauthors, 2009b: AERONET-OC: A network for the validation of ocean color primary products. *J. Atmos. Oceanic Technol.*, **26**, 1634–1651, <https://doi.org/10.1175/2009JTECHO654.1>.
- , J.-F. Berthon, F. Mélin, and D. D’Alimonte, 2011: Cross-site consistent in situ measurements for satellite ocean color applications: The BiOMaP radiometric dataset. *Remote Sens. Environ.*, **115**, 2104–2115, <https://doi.org/10.1016/j.rse.2011.04.013>.
- , F. Mélin, J. F. Berthon, and M. Talone, 2015: In situ autonomous optical radiometry measurements for satellite ocean color validation in the western Black Sea. *Ocean Sci.*, **11**, 275–286, <https://doi.org/10.5194/os-11-275-2015>.